J. Mech. Phys. Solids 161 (2022) 104813

Contents lists available at ScienceDirect

Journal of the Mechanics and Physics of Solids

journal homepage: www.elsevier.com/locate/jmps

Cylindrical compressible liquid inclusion with surface effects

Fei Ti [a,b], Xin Chen [c,*], Moxiao Li [a,b], Xuechao Sun [a,b], Shaobao Liu [a,b], Tian Jian Lu [a,b,*]

[a] State Key Laboratory of Mechanics and Control of Mechanical Structures, Nanjing University of Aeronautics and Astronautics, Nanjing 210016, P. R. China

[b] MIIT Key Laboratory of Multifunctional Lightweight Materials and Structures, Nanjing University of Aeronautics and Astronautics, Nanjing 210016, P.R. China

[c] Xi'an Modern Chemistry Research Institute, Xi'an, 710065, P.R. China

ARTICLE INFO

Keywords:
Cylindrical liquid inclusion
Surface effects
Surface curvature
Effective moduli
Negative Poisson ratio

ABSTRACT

Liquid-filled microchannels are common in biological tissues, such as blood capillaries and neuronal axons, which may often be regarded as cylindrical compressible liquid inclusions embedded in an infinite elastic matrix. How surface effects influence the elastic field and effective mechanical properties of such liquid inclusions remain elusive, especially when the inclusion size is at micro level wherein surface tension plays a significant role. We present first a theoretical model to analyze the elastic field of a cylindrical compressible liquid inclusion, with surface effects duly accounted for. We then use the solutions of our model, together with the Eshelby approach, to estimate the effective mechanical properties of a composite containing sparsely distributed cylindrical liquid inclusions. Different from previous studies, our model accounts for the nonlinear dependence of the normal vector and curvature of a liquid-solid surface upon surface deformation, achieved by expressing both as first order functions of surface displacement. We then linearize the deformation-induced surface curvature to simplify the problem and get the solution using linearized curvature. Predictions of our model demonstrate that surface effects prevent deformation of the liquid inclusion and increase stress concentration around the inclusion. Further, as the surface energy is increased, the effective Young's modulus of the two-phase composite first increases and then decreases, and the transition point is related to the bulk modulus of liquid; when the surface energy becomes sufficiently large, the effective Poisson ratio becomes negative. These results are useful for understanding and exploring the mechanical behaviors of a wide range of liquid-filled porous biological materials which contain distributed cylindrical pores, e.g., blood vessels, neuronal axons, dentinal tubules and hydrogel pores .

1. Introduction

Materials with cylindrical inclusions exist widely in engineering and nature, such as fiber-reinforced composites (Mishnaevsky Jr and Brøndsted, 2009) and muscle tissues (Armstrong and Phelps, 1984). On the one hand, as these materials are usually used to bear loads or transfer forces in practical applications, their effective mechanical properties have long become the research focus. On the other hand, the elastic fields around the inclusion(s) are also important and have been extensively exploited. For example, neuronal

* Corresponding authors.
E-mail addresses: xinchern@126.com (X. Chen), tjlu@nuaa.edu.cn (T.J. Lu).

https://doi.org/10.1016/j.jmps.2022.104813
Received 20 October 2021; Received in revised form 15 January 2022; Accepted 7 February 2022
Available online 8 February 2022
0022-5096/© 2022 Elsevier Ltd. All rights reserved.

axons in brain may be regarded as cylindrical inclusions, such that the elastic fields around neuronal axons can significantly affect their biological functions (Mutalik and Ghose, 2020).

In continuum mechanics, theoretical studies of the inclusion problem dated back to Goodier (1933) and Love (1944), followed by Eshelby (1957) who derived the elastic fields of an ellipsoidal inclusion. Subsequently, Hasegawa et al. (1992) proved that the problem of a cylindrical inclusion is a limiting case of the ellipsoidal inclusion, i.e., when its major axis tends to infinity. Besides, the elastic fields of a cylindrical inclusion are extended to study stress concentration (Hwu and Ting, 1989), effective mechanical properties (Christensen and Lo, 1979) and dynamic problems (Cheng and Batra, 1999). In the last two decades, materials embedded with nearly round cross-sectional ducts (i.e., cylindrical liquid inclusions) (Bejan, 1999, 2000), have attracted much attention: for typical instance, microvascular bundles in the stems of plants (Min et al., 2015), dentin tubules in teeth (Lin et al., 2011; Zandim et al., 2004), Haver's tubules in bone (Frame et al., 2018), blood capillaries (Harrison et al., 2002), microchannels in hydrogels (Huang et al., 2011), and flexible electronics devices (Frutiger et al., 2015). Materials having cylindrical liquid inclusions exhibit multifunctional attributes, such as mechanical support, mass transfer and heat transfer. In fact, in both nature and engineering, many materials require multi-functional properties, with the mechanical behavior of the material often playing a vital role. Therefore, it is necessary to not only investigate how the materials with liquid inclusions perform mechanically when external loads are applied, but also explore the underlying mechanisms.

It is important to clarify the properties of the liquid before considering the mechanical behaviors of liquid inclusions. As stated by Rice (Britannica, 1993), "A material is called solid rather than fluid if it can also support a substantial shearing force over the time scale of some natural process or technological application of interest." Built upon the equivalent method (Eshelby, 1957), Chen et al. (2018) demonstrated that a liquid inclusion can be regarded as a special solid inclusion without shear modulus under quasi-static conditions without surface effects. Thus, in the absence of surface effects, the elastic fields of a cylindrical liquid inclusion can be degenerated from that of the solid inclusion.

For a microscale liquid inclusion embedded in an elastic matrix, although the liquid can still be regarded as a special solid, the liquid-solid interface is intrinsically different from the interface between different solids. Gurtin and Murdoch (1975) presented a continuum description of the interface between different materials and established a second-order tensor on the material surface (interface) named surface stress $\boldsymbol{\sigma}_s$ to describe the surface effects. When the surface experiences deformation, the surface stress is related to surface energy γ as (Nix and Gao, 1998; Sharma et al., 2003):

$$\boldsymbol{\sigma}_s = \gamma \mathbf{I} + \frac{\partial \gamma}{\partial \boldsymbol{\varepsilon}_s}, \tag{1}$$

where the first term stems from the variation of atom number per unit area of the surface, $\mathbf{I}$ is the unit tensor on the surface, and the second term comes from surface energy variation per atom on the surface. As the second term is induced by changes in atomic spacing, it also represents a variation of surface energy with respect to elastic strain $\boldsymbol{\varepsilon}_s$. For a solid-solid surface, the first term is about an order of magnitude smaller than the second one (Krichen et al., 2019), thus usually neglected (Duan et al., 2005, 2007; Ru et al., 2009). In sharp contrast, for a liquid-solid surface, the first term dominates the second term, so the latter is usually neglected (Style et al., 2015). This is because the surface energy per atom approaches a constant when the liquid-solid surface deforms, and hence the surface stress σ_s only depends on the variation of atom number on the surface, i.e., the area of the deformed surface. It follows that, for a microscale cylindrical liquid inclusion with surface effects (Chuanren et al., 2004; Harrison et al., 2002; Huang et al., 2012, 2011; Zandim et al., 2004), relevant elastic fields cannot be degenerated from those of a solid inclusion.

Force equilibrium at a liquid-solid surface can be expressed as (Gurtin and Murdoch, 1975):

$$\boldsymbol{\sigma} \cdot \mathbf{n} + p\mathbf{n} = \gamma\kappa\mathbf{n}, \tag{2}$$

where $\boldsymbol{\sigma}$ is the stress in solid matrix, $\mathbf{n}$ is the normal vector of the surface, p is the total liquid pressure, κ is the surface curvature, and $\gamma\kappa$ is the surface tension. Eq. (2) is often called the Young-Laplace equation (Style et al., 2015). Note that the force balance of Eq. (2) has two properties: (1) both the pressure and surface tension are along the normal direction; (2) the curvature depends on surface deformation. In other words, the force balance is dependent upon surface deformation. In fact, the force balance of Eq. (2) is essential for studying liquid-solid surfaces, as suggested by the Rayleigh-Plateau instability (*i.e.*, a liquid inclusion becomes sausage-like) (Mora et al., 2010). Several studies have estimated the critical value of surface tension when the Rayleigh-Plateau instability occurs by analytical methods (Cheewaruangroj et al., 2019; Xuan and Biggins, 2015) and simulation methods (Henann and Bertoldi, 2014). As for cylindrical liquid inclusions with surface effects, there have been a few theoretical studies. However, the surface models in these studies (*e.g.*, (Dai, Li and Schiavone, 2018; Wu et al., 2018)adopted mathematical expressions for deformation-induced change in surface curvature that either neglected the influence of uniform/non-uniform surface displacement on surface curvature, or could not predict the singularity of a liquid inclusion when its surface energy is large enough. For instance, focusing upon an elliptical liquid inclusion embedded in an infinite elastic matrix, Wu et al., (2018) analyzed the effects of surface on stress concentration and liquid pressure, and then used the results to estimate the effective Young's modulus of a composite containing cylindrical liquid inclusions. Nonetheless, in this study, the effects of uniform as well as non-uniform deformation on surface curvature were neglected, which may lead to significant prediction errors when surface effects are of concern; more details are presented in Section 3.1. In another study (Dai et al., 2018), explicit analytical solution was presented for a cylindrical compressible liquid inclusion in an infinite elastic matrix, which was then employed to quantify stress concentration around the inclusion under plane deformation based on the complete Gurtin–Murdoch interface model. Their solutions nonetheless do not predict any singularity induced by large surface energy. Xuan and Biggins (2015) demonstrated that, when surface energy is sufficiently large, the assumption of plane strain does not hold. Therefore, a

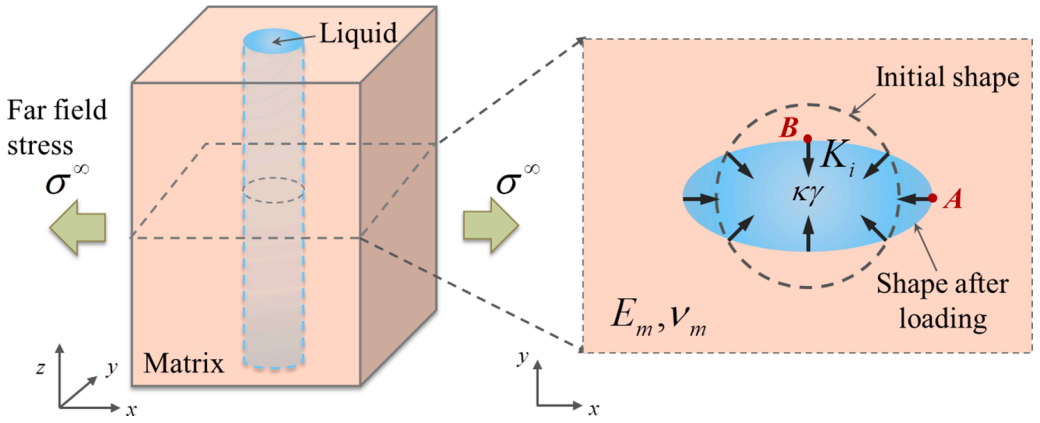

Fig. 1. Schematic of a cylindrical compressible liquid inclusion embedded in an infinite matrix. The bulk modulus of the liquid inclusion is K_i, and the Young's modulus and Poisson ratio of the matrix are E_m and ν_m, respectively. Between the inclusion and the matrix is surface tension, where κ is the curvature of the surface and γ is the surface energy. There is a far field stress σ^∞ applied at infinity of the matrix. The dashed line and the elliptical part represent the initial shape of the liquid inclusion and its shape under far-field stressing, respectively.

more accurate surface model accounting for the influence of surface deformation on curvature is needed to analyze the elastic fields around a cylindrical compressible liquid inclusion and estimate the effective elastic moduli of a two-phase composite containing distributed cylindrical compressible liquid inclusions.

We propose an analytical model of cylindrical compressible liquid inclusion embedded in an infinite elastic matrix. With surface effects on liquid-solid surface duly considered, we present the governing equations and boundary conditions in Section 2. In Section 3, we first linearize the deformation-induced curvature of liquid-solid surface to simplify the problem and then get the solution of the problem using the linear curvature. The solution is compared with that of Wu et al. (Wu et al., 2018). In Section 4, we analyze the deformation of the inclusion as well as stress concentration around the inclusion. Effective mechanical properties of the composite with cylindrical liquid inclusions are given in Section 5. Finally, we give a discussion of the solution in Section 6.

2. Problem statement

Starting from a cylindrical compressible liquid inclusion of radius R embedded in an infinite solid matrix (Fig. 1), we focus on its in-plane response such that the problem can be simplified to plane strain. With the solid assumed to be isotropic linear elastic, its governing equations are:

$$\begin{aligned} \boldsymbol{\varepsilon} &= \frac{1}{2}(\nabla \mathbf{u} + \mathbf{u}\nabla), \\ \boldsymbol{\sigma} &= \lambda \mathrm{tr}(\boldsymbol{\varepsilon}) + 2G\boldsymbol{\varepsilon}, \\ \nabla \cdot \boldsymbol{\sigma} &= 0, \end{aligned} \tag{3}$$

where $\mathbf{u}$, $\boldsymbol{\varepsilon}$ and $\boldsymbol{\sigma}$ are the displacement, strain and stress in the solid matrix, respectively, and λ (N/m^2) and G (N/m^2) are Lame constants of the solid material.

Let the liquid be linearly compressible, such that (Shafiro and Kachanov, 1997):

$$K_i \frac{\Delta V}{V_0} = -p_{load}, \tag{4}$$

where K_i (N/m^2) is the bulk modulus of the liquid, V_0 and ΔV are the initial volume and volumetric change of the liquid inclusion, and p_{load} is the change of liquid pressure due to external loading. Note that the total liquid pressure $p = p_0 + p_{load}$, p_0 being the initial liquid pressure.

When a far field stress $\boldsymbol{\sigma}^\infty$ is applied, the stress at infinity satisfies:

$$\boldsymbol{\sigma}|_{|\mathbf{x}|\to\infty} = \boldsymbol{\sigma}^\infty. \tag{5}$$

With particular focus placed upon in-plane (i.e., the x-y plane) behaviors of the liquid inclusion, $\boldsymbol{\sigma}^\infty$ is uniform along the z-axis direction (i.e., the axial direction of liquid inclusion).

Force equilibrium on the liquid-solid surface is given by the Young-Laplace equation, i.e., Eq. (2) (Style et al., 2015). The first and second terms of the left hand side of Eq. (2) stem from the solid and liquid, respectively, while the term of the right hand side comes from the surface. It should be pointed out that the present analysis considers the fact that both $\mathbf{n}$ and κ depend on the deformation of the surface, which is different from previous studies (Fischer et al., 2008; Yang, 2004), as discussed later in Section 3. In fact, both $\mathbf{n}$ and κ are nonlinear functions of surface displacement (Do Carmo, 1976), thus making it difficult to solve the problem. To obtain a solution of

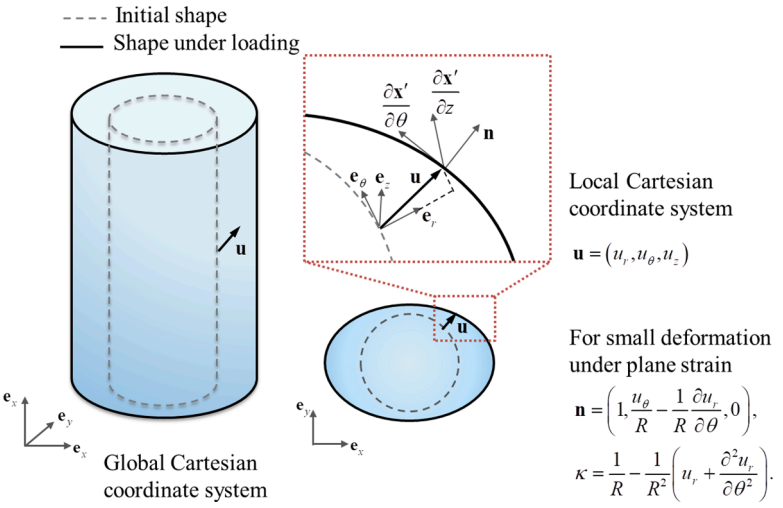

Fig. 2. Influence of surface deformation on curvature. The dashed line represents the initial shape of the cylindrical cylinder, while the solid line represents its shape under load. $\mathbf{u}$ is the displacement of the cylindrical surface, measured in a local Cartesian coordinate system. $'$ is the location of the surface under deformation in a global Cartesian coordinate system. $\frac{\partial'}{\partial\theta}$ and $\frac{\partial'}{\partial z}$ are the tangents on the deformed surface in the θ and z directions, respectively. $\mathbf{n}=\left(1,\frac{u_\theta}{R}-\frac{1}{R}\frac{\partial u_r}{\partial\theta},0\right)$ is the normal vector and $\kappa=\frac{1}{R}-\frac{1}{R^2}\left(u_r+\frac{\partial^2 u_r}{\partial\theta^2}\right)$ is the curvature under plane-strain small deformation. $\mathbf{e}_r,\mathbf{e}_\theta,\mathbf{e}_z$ are base vectors of the local Cartesian coordinate system, and $\mathbf{e}_x,\mathbf{e}_y,\mathbf{e}_z$ are base vectors of the global Cartesian coordinate system.

the problem, under the assumption of small deformation, we express both $\mathbf{n}$ and κ as first order functions of surface displacement.

3. Solution of the problem

Where ever there is a material surface, surface stress (surface tension) is present no matter whether or not a far field load $\boldsymbol{\sigma}^\infty$is applied. However, although surface tension can cause a residual stress field in the absence of $\boldsymbol{\sigma}^\infty$, here we only focus on the elastic fields induced by $\boldsymbol{\sigma}^\infty$. To this end, we first derive the surface normal vector and the curvature and express them as functions of surface displacement, and then linearize them to simplify the equilibrium of liquid-solid surface.

3.1. Expressions of surface normal vector and curvature

To simply the boundary condition of Eq. (2), we need expressions of the normal vector $\mathbf{n}$ and curvature κ in terms of surface deformation. In this part, we first present geometrical analysis of the deformation of a cylinder and express $\mathbf{n}$ and κ as functions of surface displacement. Then, for simplification, we linearize these expressions under the assumption of small deformation.

Consider a cylinder of radius R set in a (global) cylindrical polar coordinate system (Fig. 2). Its surface has an initial curvature of $\frac{1}{R}$. In the presence of external loading, assume the surface deforms with displacement field $\mathbf{u}=(u_r,u_\theta,u_z)$, which is measured in a local Cartesian coordinate system (Fig. 2). In the global Cartesian coordinate system, each point on the undeformed cylindrical surface can be expressed as $\mathbf{x}=(R\cos\theta,R\sin\theta,z)$. As the surface deforms, it moves to:

$$\begin{aligned}\mathbf{x}' &= \mathbf{x}+\mathbf{u}\cdot\mathbf{T}\\ &= (R\cos\theta+u_r\cos\theta-u_\theta\sin\theta,R\sin\theta+u_r\sin\theta+u_\theta\cos\theta,z+u_z),\end{aligned}\tag{6}$$

where

$$\mathbf{T}=\begin{bmatrix}\cos\theta & \sin\theta & 0\\ -\sin\theta & \cos\theta & 0\\ 0 & 0 & 1\end{bmatrix},\tag{7}$$

is a 3×3 matrix representing the transformation from local to global Cartesian coordinate system (Fig. 2).

On the deformed surface of the cylinder, the tangent in the θ direction is:

$$\frac{\partial \mathbf{x}'}{\partial \theta} = \begin{pmatrix} -R\sin\theta - u_r\sin\theta - u_\theta\cos\theta + \dfrac{\partial u_r}{\partial \theta}\cos\theta - \dfrac{\partial u_\theta}{\partial \theta}\sin\theta \\ R\cos\theta + u_r\cos\theta - u_\theta\sin\theta + \dfrac{\partial u_r}{\partial \theta}\sin\theta + \dfrac{\partial u_\theta}{\partial \theta}\cos\theta \\ \dfrac{\partial u_z}{\partial \theta} \end{pmatrix}^T. \tag{8}$$

while that in the z direction is:

$$\frac{\partial \mathbf{x}'}{\partial z} = \begin{pmatrix} \dfrac{\partial u_r}{\partial z}\cos\theta - \dfrac{\partial u_\theta}{\partial z}\sin\theta \\ \dfrac{\partial u_r}{\partial z}\sin\theta + \dfrac{\partial u_\theta}{\partial z}\cos\theta \\ 1 + \dfrac{\partial u_z}{\partial z} \end{pmatrix}^T. \tag{9}$$

According to differential geometry of surface (Do Carmo, 1976), the normal vector $\mathbf{n}$ of a deformed surface can be calculated by taking the cross-product of surface tangent vectors, $\frac{\partial \mathbf{x}'}{\partial \theta}$ and $\frac{\partial \mathbf{x}'}{\partial z}$, as

$$\mathbf{n} = \frac{\frac{\partial \mathbf{x}'}{\partial \theta} \times \frac{\partial \mathbf{x}'}{\partial z}}{\left|\frac{\partial \mathbf{x}'}{\partial \theta} \times \frac{\partial \mathbf{x}'}{\partial z}\right|}. \tag{10}$$

The surface curvature κ can be calculated by using the first and second fundamental forms of the surface in differential geometry (Do Carmo, 1976), as:

$$\kappa = \frac{eG - 2fF + gE}{EG - F^2}, \tag{11}$$

where E, F, G and e, f, g are separately the coefficients of the first and second fundamental forms:

$$E = \frac{\partial x'}{\partial \theta} \cdot \frac{\partial x'}{\partial \theta}, F = \frac{\partial x'}{\partial \theta} \cdot \frac{\partial x'}{\partial z}, G = \frac{\partial x'}{\partial z} \cdot \frac{\partial x'}{\partial z} \tag{12}$$

$$e = \mathbf{n} \cdot \frac{\partial^2 \mathbf{x}'}{\partial \theta^2}, f = \mathbf{n} \cdot \frac{\partial^2 \mathbf{x}'}{\partial \theta \partial z}, g = \mathbf{n} \cdot \frac{\partial^2 \mathbf{x}'}{\partial^2 z}. \tag{13}$$

The first fundamental form is defined as

$$d\mathbf{x}' \cdot d\mathbf{x}' = Ed\theta^2 + 2Fd\theta dz + Gdz^2, \tag{14}$$

and the second fundamental form is defined as

$$\mathbf{n} \cdot d^2\mathbf{x}' = ed\theta^2 + 2fd\theta dz + gdz^2. \tag{15}$$

Eqs. (10) and (11) suggest that both $\mathbf{n}$ and κ are nonlinear functions of surface displacement $\mathbf{u}$, which makes it difficult to consider surface effects in any theoretical analysis. To address the issue, we simplify the expressions of Eqs. (10) and (11) for the cylindrical problem of concern, as elucidated below.

Firstly, the present problem is plane strain, so there exists no strain in the z direction. The in-plane displacements u_r and u_θ are uniform along the z direction, that is:

$$\begin{aligned} &u_z = \text{constant}, \\ &\frac{\partial u_r}{\partial z} = 0, \\ &\frac{\partial u_\theta}{\partial z} = 0. \end{aligned} \tag{16}$$

Secondly, because the local coordinate system is defined in the undeformed cylinder configuration, it is rotation-invariant with respect to θ and translation-invariant with respect to z. To calculate the normal vector and curvature, surface displacements expressed in local coordinates are employed. Due to the rotation-invariant and translation-invariant attributes, the results of Eqs. (10) and (11) for point $(R, 0, z)$, z being arbitrary, also hold for other points with nonzero θ. Alternatively, if we want to calculate the normal vector and curvature of a certain point, we might as well select the global coordinate system so that the coordinates of this point are $(R, 0, z)$). Setting $\theta = 0$, $z = 0$ and combining Eq. (16), we rewrite Eqs. (8) and (9) as:

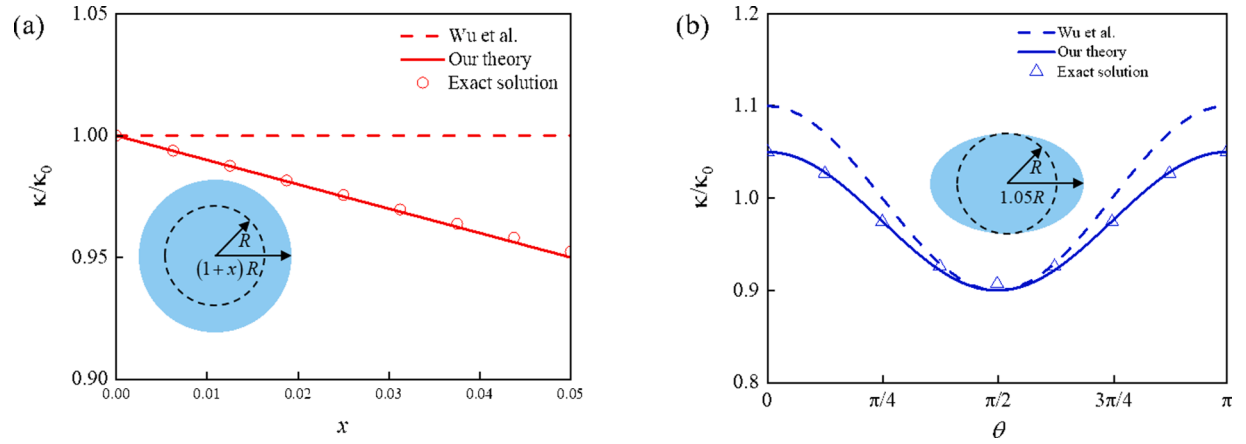

Fig. 3. Influence of surface deformation on surface curvature: comparison between predictions obtained using the present and existing theoretical models (Do Carmo, 1976; Wu et al., 2018). (a) Uniform deformation. The circle of initial radius R becomes a circle with radius $(1+x)R$ as, in this case, only uniform deformation $\frac{u_r}{R^2}$ affects the surface curvature. (b) Non-uniform deformation. The circle of initial radius R becomes an ellipse with major axis 1.05R and minor axis R as, in this case, only non-uniform deformation $\frac{1}{R^2}\frac{\partial^2 u_r}{\partial\theta^2}$ affects the surface curvature of the minor axis of the ellipse.

$$\frac{\partial \mathbf{x}'}{\partial\theta}=\begin{pmatrix}-u_\theta+\dfrac{\partial u_r}{\partial\theta}\\ R+u_r+\dfrac{\partial u_\theta}{\partial\theta}\\ 0\end{pmatrix}^T \text{ and } \frac{\partial \mathbf{x}'}{\partial z}=\begin{pmatrix}0\\0\\1\end{pmatrix}^T. \tag{17}$$

Taking the derivative of Eqs. (8) and (9), making use of Eq. (16), and setting $\theta=0$ and $z=0$, we arrive at:

$$\frac{\partial^2 \mathbf{x}'}{\partial\theta^2}=\begin{pmatrix}-R-u_r-2\dfrac{\partial u_\theta}{\partial\theta}+\dfrac{\partial^2 u_r}{\partial\theta^2}\\ 2\dfrac{\partial u_r}{\partial\theta}-u_\theta+\dfrac{\partial^2 u_\theta}{\partial\theta^2}\\ 0\end{pmatrix}^T, \frac{\partial^2 \mathbf{x}'}{\partial\theta\partial z}=\begin{pmatrix}0\\0\\0\end{pmatrix}^T, \frac{\partial^2 \mathbf{x}'}{\partial z^2}=\begin{pmatrix}0\\0\\0\end{pmatrix}^T. \tag{18}$$

Thirdly, we linearize the expressions of Eqs. (10) and (11) for displacement **u** when the surface undergoes small deformation. With the second or higher order of **u** neglected, the normal vector is simplified to:

$$\mathbf{n}=\left(1,\frac{u_\theta}{R}-\frac{1}{R}\frac{\partial u_r}{\partial\theta},0\right), \tag{19}$$

Similarly, the curvature becomes:

$$\kappa=\frac{1}{R}-\frac{1}{R^2}\left(u_r+\frac{\partial^2 u_r}{\partial\theta^2}\right), \tag{20}$$

where the first term is the initial curvature and the second term is the change of curvature due to deformation.

It follows from Eqs. (19) and (20) that, in the absence of displacement, the normal vector and curvature will be $(1,0,0)$ and $\frac{1}{R}$. In the presence of displacement, as a result of uniform deformation $\frac{u_r}{R^2}$ and non-uniform displacement $\frac{1}{R^2}\frac{\partial^2 u_r}{\partial\theta^2}$, the second component of the normal vector is no longer null. The curvature is the reciprocal of curvature radius, which means that the displacement along the circumference (i.e., u_θ) will not affect the curvature under small deformation. The curvature is therefore only related to the radial displacement u_r. For the case when u_r is independent of θ, the normal vector does not change, and the curvature is given by $\frac{1}{R}-\frac{u_r}{R^2}$. In a previous study (Wu et al., 2018), the curvature was expressed as $\frac{1}{R}-\frac{1}{R^2}\frac{\partial^2 u_r}{\partial\theta^2}$, which is oversimplified because neglecting the contribution of uniform deformation $\frac{u_r}{R^2}$ to curvature can lead to significant prediction errors.

To validate the linear expression of surface curvature, we compare our results with the exact solution (Do Carmo, 1976) and the result of Wu et al. (Wu et al., 2018) for two cases, i.e., uniform surface deformation and non-uniform surface deformation. For a deforming plane curve $\alpha(\theta)=(x(\theta),y(\theta))$, the exact solution of its curvature for both cases is given by (Do Carmo, 1976):

$$\kappa = \frac{\frac{\partial x}{\partial \theta}\frac{\partial^2 y}{\partial \theta^2} - \frac{\partial^2 x}{\partial \theta^2}\frac{\partial y}{\partial \theta}}{\left[\left(\frac{\partial x}{\partial \theta}\right)^2 + \left(\frac{\partial y}{\partial \theta}\right)^2\right]^{\frac{3}{2}}}. \tag{21}$$

In a previous study of cylindrical liquid inclusion (Wu et al., 2018), the surface curvature is calculated by:

$$\kappa = \frac{1}{R} - \frac{1}{R^2}\frac{\partial^2 u_r}{\partial \theta^2}, \tag{22}$$

Before deformation, let a circle of radius R represent the plane curve of concern. We compare in Fig. 3 surface curvature predictions obtained using the present and existing theoretical models (Do Carmo, 1976; Wu et al., 2018). For the case of uniform deformation, we assume the circle deforms with the following displacements:

$$\begin{aligned} u_r &= xR, \\ u_\theta &= 0, \end{aligned} \tag{23}$$

such that, upon deformation, the circle remains a circle but exhibits an enlarged radius xR Using Eqs. (20), (21) and (22), we obtain surface curvatures using different calculation methods, as:

$$\begin{aligned} \kappa_1 &= \frac{1-x}{R} \\ \kappa_2 &= \frac{1}{R(1+x)} \\ \kappa_3 &= \frac{1}{R} \end{aligned} \tag{24}$$

In the following, to ensure the assumption of small deformation, the maximum value of $\frac{u_r}{R}$ is set as 0.05. As shown in Fig. 3(a), for a displacement of $\frac{u_r}{R} = 0.05$, the prediction obtained using the curvature expression of Eq. (22) has an error of ~5% compared with the exact solution, while the present model prediction has a marginal error of ~0.3%.

For the case of non-uniform deformation, we assume that the circle of initial radius R deforms according to:

$$\begin{aligned} u_r &= 0.025R(1+\cos 2\theta), \\ u_\theta &= 0.025R\sin 2\theta. \end{aligned} \tag{25}$$

After deformation, the circle becomes an ellipse with a major axis 1.05R and a minor axis R. As shown in Fig. 3(b), the prediction obtained with Eq. (22) has a maximum error of ~5% relative to the exact solution, while the present model prediction exhibits a much smaller error of ~0.8%. Although the differences of different theories are not large, the theory of Wu et al. lacks the uniform effect induced by hydrostatic deformation (Style et al., 2015), which implies surface tension does not influence the inclusion behaviors when hydrostatic deformation is applied.

It should be mentioned that the linearized normal vector and curvature of Eqs. (19) and (20) are valid for plane-strain small deformation, which are adopted to get the solution of the problem, as demonstrated below.

3.2. Elastic fields

In the absence of external loading, both the solid matrix and the liquid inclusion are in the residual stress state. Linear elasticity dictates that residual stresses induced by surface effects should be balanced before and after loading (Huang and Wang, 2013). Therefore, residual stress will not change the solution of elastic fields induced by far field load. In the present study, to simplify the boundary conditions, we chose a simplest stress state, i.e., residual stresses are not present in the solid matrix. In fact, previous studies of spherical liquid inclusions with surface effects also use the assumption that the residual stress is balanced with liquid pressure (Mancarella et al., 2016; Style et al., 2015). Hence, the assumption that, initially, the liquid has a residual stress of $p_0 = \frac{\gamma}{R}$ while no stress is present in the solid matrix is adopted to solve the problem of Fig. 1. Accordingly, a general solution of displacement fields in the solid can be expressed as (Love, 1944; Timoshenko and Goodier, 1951):

$$\begin{aligned} u_r &= B_1 r + B_2\frac{R^2}{r} + \cos(2\theta)\left[2\nu_m A_1\frac{r^3}{R^2} - 2A_2 r + 4(1-\nu_m)A_3\frac{R^2}{r} + 2A_4\frac{R^4}{r^3}\right], \\ u_\theta &= \sin(2\theta)\left[(-3+2\nu_m)A_1\frac{r^3}{R^2} + 2A_2 r + 2(2\nu_m - 1)A_3\frac{R^2}{r} + 2A_4\frac{R^4}{r^3}\right]. \end{aligned} \tag{26}$$

Corresponding stress fields in the solid are

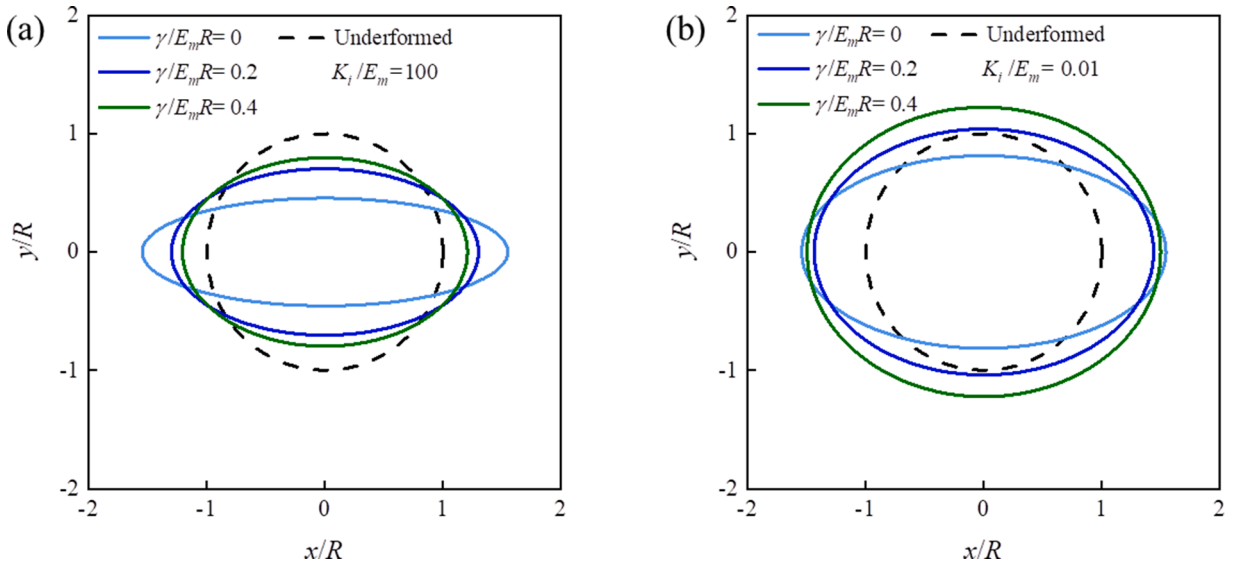

Fig. 4. Shape of deformed cylindrical compressible liquid inclusion under uniaxial stretching. (a) $K_i/E_m = 100$ (displacements magnified 10×); the inclusion can be taken as approximately incompressible, since surface tension is small in relation to liquid compressibility. (b) $K_i/E_m = 0.01$; the liquid inclusion can be taken as a cavity. Different colors represent different surface effects. $\nu_m = 0.3$ and $\varepsilon^\infty = 0.02$ are selected for the plotting.

$$\begin{aligned}
\sigma_{rr} &= \frac{E_m}{1+\nu_m}\left[\frac{B_1}{1-2\nu_m} - B_2\frac{R^2}{r^2} - \cos(2\theta)\left(2A_2 + 4A_3\frac{R^2}{r^2} + 6A_4\frac{R^4}{r^4}\right)\right],\\
\sigma_{\theta\theta} &= \frac{E_m}{1+\nu_m}\left[\frac{B_1}{1-2\nu_m} + B_2\frac{R^2}{r^2} - \cos(2\theta)\left(6A_1\frac{r^2}{R^2} - 2A_2 - 6A_4\frac{R^4}{r^4}\right)\right],\\
\sigma_{r\theta} &= \frac{E_m}{1+\nu_m}\sin(2\theta)\left(-3A_1\frac{r^2}{R^2} + 2A_2 - 2A_3\frac{R^2}{r^2} - 6A_4\frac{R^4}{r^4}\right),
\end{aligned} \tag{27}$$

where E_m and ν_m are the Young's modulus and Poisson ratio of the solid material, respectively.

Given that the solution obtained under uniaxial stretching can be used to derive solutions for other types of external loading, particular focus is placed upon this solution. The far field boundary condition (5) can thus be written as:

$$\boldsymbol{\sigma}^\infty = \begin{bmatrix} \sigma^\infty & 0 & 0\\ 0 & 0 & 0\\ 0 & 0 & 0 \end{bmatrix}. \tag{28}$$

At the liquid-solid surface, equilibrium dictates that:

$$\boldsymbol{\sigma}\cdot\mathbf{n} + (p_0 + p_{load})\mathbf{n} = \kappa\gamma\mathbf{n}. \tag{29}$$

where $\boldsymbol{\sigma}$ and p_{load} are the stress and pressure induced by the far field load σ^∞, and κ is the curvature after deformation. It should be noted that the stress is a first order function of displacement, but the pressure is a nonlinear function of displacement, causing difficulties in obtaining an analytical solution of the problem. Therefore, for simplification, we linearize the pressure as a first order function of displacement, yielding:

$$\begin{aligned}
p_{load} &= -K_i\frac{\Delta V}{V_0} = -K_i\frac{\pi[R + u_r(r=R,\theta=0)]\left[R + u_r\left(r=R,\theta=\frac{\pi}{2}\right)\right] - \pi R^2}{\pi R^2}\\
&= -K_i\frac{u_r(r=R,\theta=0) + u_r\left(r=R,\theta=\frac{\pi}{2}\right)}{R}.
\end{aligned} \tag{30}$$

With Eqs. (19), (20) and (30), Eq. (29) becomes:

$$\begin{bmatrix} \sigma_{rr} + \frac{\sigma_{r\theta}}{R}\left(u_\theta - \frac{\partial u_r}{\partial\theta}\right)\\ \sigma_{r\theta} + \frac{\sigma_{\theta\theta}}{R}\left(u_\theta - \frac{\partial u_r}{\partial\theta}\right) \end{bmatrix} + \begin{bmatrix} p_0 + p\\ \frac{p_0+p}{R}\left(u_\theta - \frac{\partial u_r}{\partial\theta}\right) \end{bmatrix} = \frac{\gamma}{R}\begin{bmatrix} 1 - \frac{1}{R}\left(u_r + \frac{\partial^2 u_r}{\partial\theta^2}\right)\\ u_\theta - \frac{\partial u_r}{\partial\theta} \end{bmatrix}. \tag{31}$$

Substituting $p_0 = \frac{\gamma}{R}$ into (31) and neglecting the second order terms under the assumption of plane-strain small deformation, we

arrive at:

$$\begin{bmatrix}\sigma_{rr}\\ \sigma_{r\theta}\end{bmatrix}+\begin{bmatrix}p\\ 0\end{bmatrix}=\frac{\gamma}{R}\begin{bmatrix}(\kappa-\kappa_0)\\ 0\end{bmatrix}. \tag{32}$$

where $\gamma(\kappa-\kappa_0)=-\frac{\gamma}{R}\left(u_r+\frac{\partial^2 u_r}{\partial\theta^2}\right)$ is the change in surface tension induced by far field stressing.

From the far field boundary condition (28) and the surface boundary condition (32), it follows that:

$$\begin{aligned}
B_1&=\frac{1-\nu_m-2\nu_m^2}{2}\frac{\sigma^\infty}{E_m},\\
B_2&=\frac{(1+\nu_m)\left[\left(-1+\nu_m+2\nu_m^2\right)\left(\frac{L}{R}-2\frac{K_i}{E_m}\right)-1\right]}{2\left[(1+\nu_m)\left(\frac{L}{R}-2\frac{K_i}{E_m}\right)-1\right]}\frac{\sigma^\infty}{E_m},\\
A_1&=0,\\
A_2&=-\frac{(1+\nu_m)}{4}\frac{\sigma^\infty}{E_m},\\
A_3&=\frac{(1+\nu_m)\left[(1+\nu_m)\frac{L}{R}-1\right]}{2\left[\left(-5+\nu_m+6\nu_m^2\right)\frac{L}{R}-1\right]}\frac{\sigma^\infty}{E_m},\\
A_4&=-\frac{(1+\nu_m)\left[\left(-1+\nu_m+2\nu_m^2\right)\frac{L}{R}-1\right]}{4\left[\left(-5+\nu_m+6\nu_m^2\right)\frac{L}{R}-1\right]}\frac{\sigma^\infty}{E_m}.
\end{aligned} \tag{33}$$

where $L=\gamma/E_m$ is the elastocapillary length (Style et al., 2015), and L/R is a dimensionless parameter characterizing surface effects. When $L/R\to 0$, surface effects can be neglected. While B_1 and B_2 influence radial deformation (which is related to volume change), A_1, A_2, A_3 and A_4 influence shear deformation (which is related to shape change). Besides, B_2, A_3 and A_4 are related to far field load, liquid compressibility and surface effects, but B_1 and A_2 are only related to far field load. This means that surface effects affect not only radial deformation but also hoop deformation, while liquid compressibility only affects radial deformation. Note that B_2 may be singular, which is actually related to the Rayleigh-Plateau instability of liquid inclusion induced by surface tension, i.e., the liquid inclusion becomes sausage-like (Xuan and Biggins, 2015). When B_2 is nonsingular, the liquid inclusion is stable. More details of Rayleigh-Plateau instability will be presented in Section 4.1 regarding the results presented Fig. 4. In sharp contrast, the solutions reported in previous studies of cylindrical liquid inclusions (e.g., (Wu et al., 2018) do not exhibit any singularity induced by surface effects). For the case when u_r is independent of θ, this is likely attributed to the neglection of the term u_r/R^2 in the expression of surface curvature ((Wu et al., 2018), as discussed above in Section 3.1).

For illustration, an explicit expression for the displacement of point B (Fig. 1) is obtained as:

$$u_r(r=R,\theta=\pi/2)=\frac{\left(1-\nu_m^2\right)\left[1+\left(-7-\nu_m+6\nu_m^2\right)\frac{\gamma}{E_mR}+4(1+\nu_m)\frac{K_i}{E_m}\right]}{\left[1-\left(-5+\nu_m+6\nu_m^2\right)\frac{\gamma}{E_mR}\right]\left[-1+(1+\nu_m)\frac{\gamma}{E_mR}-2(1+\nu_m)\frac{K_i}{E_m}\right]}\frac{\sigma^\infty}{E_m}. \tag{34}$$

The influence of liquid compressibility on this displacement is presented in Fig. A1 of the Appendix A. In the absence of surface effects, the present predictions agree well with existing results (Berli et al., 2006).

4. Result and discussion

4.1. Inclusion deformation

To study how a cylindrical compressible liquid inclusion deforms when subjected to uniaxial stretching, the predicted variation of its shape with surface tension is presented in Fig. 4. For the plotting, two different liquid bulk moduli are selected, i.e., $K_i/E_m=100$ in Fig. 4(a) and $K_i/E_m=0.01$ in Fig. 4(b), which approach to the limiting cases of cylindrical cavity and incompressible liquid, respectively. To ensure the cylindrical liquid inclusion deforms in a stable manner, the value of γ/E_mR is varied from 0 to 0.4.

For both cases, i.e., $K_i/E_m=100$ and $K_i/E_m=0.01$, the results of Fig. 4 demonstrate that surface effects hinder the deformation of liquid inclusion. Nonetheless, as shown in Fig. 4(b), when the surface energy is sufficiently large (e.g., $\gamma/E_mR=0.4$) and the liquid bulk modulus is sufficiently small (e.g., $K_i/E_m=0.01$), the liquid inclusion exhibits an auxetic effect, namely, it expands (rather than contracts) in the transverse direction under uniaxial stretching. In contrast, such auxeticity vanishes when the liquid modulus is large, e.g., $K_i/E_m=100$. In fact, Eq. (34) indicates that the value of surface energy enabling a liquid inclusion to become auxetic is dependent

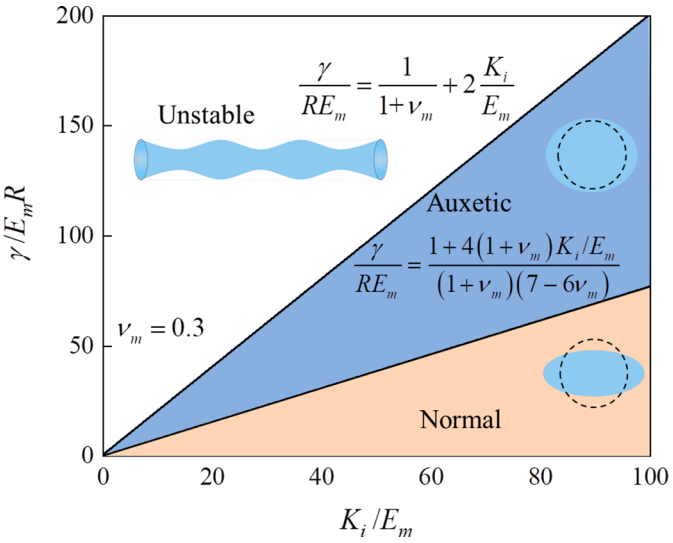

Fig. 5. Deformation states of cylindrical compressible liquid inclusion under uniaxial stretching. The phase diagram is divided into three regimes by two lines, $\frac{\gamma}{E_mR}=\frac{1+4(1+\nu_m)K_i/E_m}{(1+\nu_m)(7-6\nu_m)}$ and $\frac{\gamma}{E_mR}=\frac{1}{1+\nu_m}+2\frac{K_i}{E_m}$, which determine inclusion auxeticity and instability, respectively. The free end of the inclusion shrinks in the first regime but expands in the second regime. Within the third regime, the solution becomes singular and the inclusion is unstable. A cylindrical cavity (i.e., $K_i/E_m=0$) becomes unstable when $\frac{\gamma}{E_mR}>\frac{1}{1+\nu_m}$, which is consistent with existing result (Xuan and Biggins, 2015). For the plotting, $\nu_m=0.3$ is selected.

upon its bulk modulus. The larger the liquid bulk modulus, the larger the surface energy needed to make the inclusion auxetic. The reason for such auxeticity is that surface effects tend to minimize the surface area. For the present two-dimensional (2D) cylindrical inclusion, surface effects tend to minimize the boundary of its cross-section. Under uniaxial stretching, its initially circular boundary becomes an ellipse. To minimize the length of the elliptical boundary, the minor axis needs to be elongated such that the boundary tends to a circle as surface tension is increased. When the surface energy becomes sufficiently large, the minor axis exceeds the initial radius, thus enabling the auxetic effect to occur. Nonetheless, we should point out that such auxetic effect is yet observed in experiments. For clarification, we collect herein the typical values of γ/E_mR for common cases, e.g., 4×10^{-6} for dentin tubules (Chakrabarti and Chaudhury, 2013; Lin et al., 2011; Ziskind et al., 2011), 4×10^{-9} for marrow cavity (Chakrabarti and Chaudhury, 2013; Fuchs et al., 2018; Kosmopoulos et al., 2009), 2×10^{-2} for capillary (Frolov et al., 2019; Rosina et al., 2007; Sarin, 2010), 10^{-5} for artery (Frolov et al., 2019; Kolkman et al., 2004; Rosina et al., 2007), 10^{-3} for lymph vessel (Chakrabarti and Chaudhury, 2013; In et al., 2021; Olszewski and Engeset, 1980) and 2×10^{-3} for microchannels in hydrogels (Chakrabarti and Chaudhury, 2013; Huang et al., 2012). Note that the values of γ/E_mR are less than 0.1 for most liquid/solids systems. When the values of γ/E_mR are much larger than 0.4, Xuan and Biggins (2015) predicted that the instability of a cylindrical cavity occurs when $\gamma/E_mR\geq1/(1+\nu_m)$. And the opposite instability (e.g., the instability of a solid cylinder) has been observed experimentally (Mora et al., 2010). For the cases considered in the present study, according to the values of γ/E_mR for normal liquid/solids systems, it would be unusual to observe auxetic effect in experiments.

The results of Eq. (34) and Fig. 4 suggest that, under uniaxial stretching, the inclusion exhibits three deformation states: normal state, auxetic state and singular (unstable) state. For clarification, the different types of inclusion deformation are plotted in the $(K_i/E_m, \gamma/E_mR)$ plane as a phase diagram (Fig. 5). According to the sign (positive versus negative) of the displacement at the free end of the inclusion (i.e., point B in Fig. 1), the boundary between the normal and auxetic states can be obtained as $\frac{\gamma}{E_mR}=\frac{1+4(1+\nu_m)K_i/E_m}{(1+\nu_m)(7-6\nu_m)}$. Further, according to whether the solution is singular or not, the boundary between auxetic and singular states is given by $\frac{\gamma}{E_mR}=\frac{1}{1+\nu_m}+2\frac{K_i}{E_m}$. Correspondingly, the $(K_i/E_m, \gamma/E_mR)$ plane is divided into three regimes. Within the first regime, the liquid inclusion becomes thinner in the free direction, i.e., $u_r(r=R,\theta=\pi/2)<0$ In the second regime, the liquid inclusion becomes thicker in the free direction, i.e., $u_r(r=R,\theta=\pi/2)>0$ In the third regime, the solution becomes singular and the inclusion is unstable.

For a cylindrical cavity i.e., $K_i/E_m=0$, the predicted boundary between auxetic and singular states is consistent with existing results. Using linear stability analysis, Xuan and Biggins (2015) found that, when the surface energy is increased such that $\frac{\gamma}{E_mR}\geq\frac{1}{1+\nu_m}$ is satisfied, a cylindrical cavity embedded in an infinite solid becomes unstable. Thus, the present study suggests that $\frac{\gamma}{E_mR}=\frac{1}{1+\nu_m}+2\frac{K_i}{E_m}$ can be taken as the critical value of surface energy for the instability of a cylindrical compressible liquid inclusion.

Finally, it should be mentioned that previous studies of cylindrical liquid inclusions (Dai et al., 2018; Wu et al., 2018) did not predict the instability phenomenon, for the dependence of surface curvature on surface displacement was oversimplified.

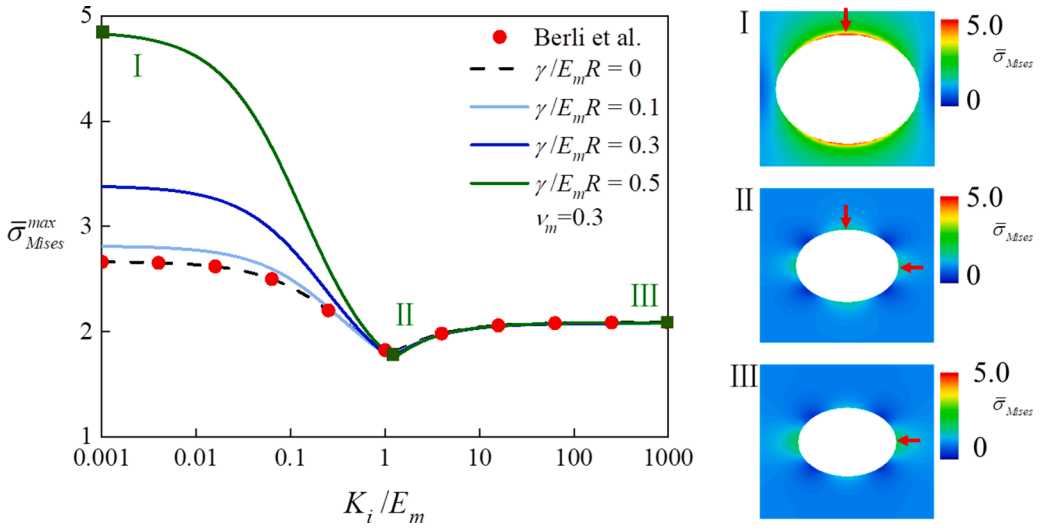

Fig. 6. Influence of liquid compressibility on stress concentration in elastic matrix under uniaxial stretching. Different lines represent different surface effects. With γ/E_mR fixed at 0.5, panels I, II and III represent separately the distribution of normalized Mises stress $\bar{\sigma}_{Mises} = \sigma_{Mises}/\sigma^{\infty}_{Mises}$ near liquid inclusion for three different values of liquid compressibility, σ^{∞}_{Mises} being the Mises stress of the far field. As liquid compressibility is increased, the location of the maximum Mises stress $\bar{\sigma}^{max}_{Mises}$ (marked by a red arrow in each panel) changes from I via II to III. When surface effects become negligible, the present prediction coincide with existing result (Berli et al., 2006). For the plotting, $\nu_m = 0.3$ is selected.

4.2. Stress concentration

Macroscopically, the strength of a two-phase composite is strongly dependent upon stress concentration induced by the inclusions (Hasselman and Fulrath, 2010). To analyze how liquid compressibility and surface energy affect stress concentration around a cylindrical compressible liquid inclusion, we plot the maximum Mises stresses in the $(\bar{\sigma}^{max}_{Mises}, K_i/E_m)$ plane (Fig. 6). (Of course, if necessary, we can also plot the maximum shear stress, or other form of stress measure, to characterize stress concentration.) Here, $\bar{\sigma}^{max}_{Mises} = \sigma^{max}_{Mises}/\sigma^{\infty}_{Mises}$, σ^{max}_{Mises} is the maximum Mises stress (i.e., stress concentration), and σ^{∞}_{Mises} is the Mises stress of the far field. In the limit when the surface effects are negligible (i.e., $\gamma/E_mR = 0$), the present predictions approach the existing results (Berli et al., 2006), thus validating in a way of our analytical model.

It is observed from Fig. 6 that, as the liquid compressibility is systematically varied, from very small (cavity) to very large (incompressible liquid), a transition point exists wherein the maximum Mises stress is minimized. In other words, there exists an optimal liquid compressibility minimizing stress concentration around the inclusion. As shown in Fig. 6, the transition occurs when the liquid bulk modulus has the same order of magnitude relative to the Young's modulus of the solid matrix, which is commonly found in biological systems. To explain the transition, for the case of $\gamma/E_mR = 0.5$, the distribution of the Mises stress around the inclusion is plotted in Fig. 6 for three different values of liquid compressibility. As the liquid compressibility is increased, the location of stress concentration (where the Mises stress is maximized) is shifted from the tip of inclusion in the free direction (point B in Fig. 1) to the load direction (point A in Fig. 1).

The results of Fig. 6 demonstrate further that, when $K_i/E_m \ll 1$, surface effects have the greatest influence on stress concentration and the maximum Mises stress increases with increasing surface energy. On one hand, the result that surface effects increase stress concentration indicates that surface effects reduce the strength of a porous material with liquid inclusions. However, how surface effects influence the strength of liquid-filled porous materials is an inconclusive question: some experiments have found that surface effects increase the strength (Jindal et al., 2016; Ozcan et al., 2001; Van Mechelen, 2004), while others have demonstrated that surface effects decrease the strength (Oshita, 2019; Vutukuri, 1974). As a result, the influence of surface effects on material strength and stress concentration is a complicated and unresolved matter that merits further investigation. This is nonetheless not the subject of the present study. On the other hand, several theoretical studies have investigated how surface effects influence stress concentration near an inclusion. The findings reveal that surface effects diminish the stress concentration when a surface model in which surface tension is not modified by surface deformation is adopted (Sharma et al., 2003). In reality, however, surface effects depend on surface deformation (Gurtin and Murdoch, 1975). Therefore, when the dependence of surface tension on surface deformation is accounted for in the surface model, surface effects are found to increase stress concentration near the inclusion (Dai et al., 2019; He and Li, 2006; Ou et al., 2008; Style et al., 2015). Thus, with the influence of surface deformation on surface tension considered, our solution about stress concentration is consistent with existing studies (Dai et al., 2019; He and Li, 2006; Ou et al., 2008; Style et al., 2015). The actual explanation behind this effect is that when you stretch, the increment of surface tension is directed outward, thus increasing the stress concentration. When $K_i/E_m > 1$, the stress concentration becomes independent of the surface effects. Note also that, when $K_i/E_m > 1$, surface effects have little influence on the Mises stress.

5. Effective mechanical properties

In physics, the essence of surface effects is attributed to the energy stored on the surface. For example, when a two-phase composite material with surface effects is loaded, the surface area will change, so the energy stored on the surface will also change. The results presented in Fig. 4 indicate that, when the dimensionless surface energy γ/E_mR is increased, surface effects on surface deformation become increasingly significant. It follows that, when γ/E_mR is large enough, surface effects become prominent in controlling the mechanical behaviors of a composite containing distributed cylindrical liquid inclusions. Therefore, in the following section, using the Eshelby approach (Eshelby, 1956, 1957; Style et al., 2015; Yang, 2004), we calculate the effective mechanical properties (i.e., Young's modulus, shear modulus and Poisson ratio) of the composite containing sparsely distributed cylindrical compressible liquid inclusions. First, we calculate the excess strain energy induced by a single liquid inclusion when the composite is subjected to different types of far field load. Then, we present explicit expressions of the effective mechanical properties and quantify how surface effects affect these properties.

5.1. Strain energy

To analyze the effective mechanical properties of the two-phase composite of concern, first we need to determine the excess energy W due to the presence of a single cylindrical liquid inclusion when it is subjected to different types of far field loading. At the far field, if the applied loads are $\sigma_{xx}^{\infty}=\sigma_1^{\infty}$ in the x-direction and $\sigma_{yy}^{\infty}=\sigma_2^{\infty}$ in the y-direction, the solution can be obtained using the liquid-solid surface boundary condition of Eq. (32), as illustrated in the Appendix B. Assuming that the strain energy of the effective medium is equal to the strain energy of the heterogeneous material Yang (2004), we obtain:

$$\begin{aligned}&\frac{1}{2E_{eff}}\left\{\left(1-\nu_{eff}^2\right)\left[\left(\sigma_1^{\infty}\right)^2+\left(\sigma_2^{\infty}\right)^2\right]-2\nu_{eff}\left(1+\nu_{eff}\right)\left(\sigma_1^{\infty}\sigma_2^{\infty}\right)\right\}\\&=\frac{1}{2E_m}\left\{\left(1-\nu_m^2\right)\left[\left(\sigma_1^{\infty}\right)^2+\left(\sigma_2^{\infty}\right)^2\right]-2\nu_m\left(1+\nu_m\right)\left(\sigma_1^{\infty}\sigma_2^{\infty}\right)\right\}+W\frac{\phi}{\pi R^2},\end{aligned}\tag{35}$$

where E_{eff} and ν_{eff} are the effective Young's modulus and effective Poisson ratio of the composite, respectively, W is the excess energy induced by one liquid inclusion, and ϕ is the volume fraction of the liquid inclusion. With no residual stress in the solid considered, the excess energy W can be written using the Eshelby formula Eshelby (1956), as:

$$W=\frac{1}{2}\int_S\left(\sigma_{ij}^{\infty}u_j-\sigma_{ij}u_j^{\infty}\right)\mathrm{d}S,\tag{36}$$

where σ_{ij} are the stresses of the elastic matrix or inclusion induced by the far field loads, σ_{ij}^{∞} are the far field stresses, u_j are the displacements of the surface, and u_j^{∞} are the far field displacements.

In the absence of liquid inclusion, the displacement and stress fields in the matrix can be expressed as:

$$\begin{aligned}u_r^{\infty}&=B_1r+\cos(2\theta)(-2A_2r),\\u_\theta^{\infty}&=\sin(2\theta)(2A_2r),\end{aligned}\tag{37}$$

$$\begin{aligned}\sigma_{rr}^{\infty}&=\frac{E_m}{1+\nu_m}\left[\frac{B_1}{1-2\nu_m}-\cos(2\theta)(2A_2)\right],\\\sigma_{r\theta}^{\infty}&=\frac{E_m}{1+\nu_m}\sin(2\theta)(2A_2).\end{aligned}\tag{38}$$

Substitution of Eqs. (26), (27), (37) and (38) into Eq. (36) gives the excess energy W due to the presence of a single inclusion, as:

$$W=\frac{2E_m\pi R^2(1-\nu_m)[B_1B_2-4(1-2\nu_m)A_2A_3]}{1-\nu_m-2\nu_m^2}.\tag{39}$$

Note that the excess energy W is expressed in a general form, suitable for the case when biaxial stretching is applied at the far field.

Finally, upon substituting Eq. (39) into Eq. (35), the effective mechanical properties of the composite containing sparsely distributed cylindrical compressible liquid inclusions are obtained.

5.2. Effective shear modulus

When the far field load is pure shear (i.e., $\sigma_1^{\infty}=\sigma^{\infty}$, $\sigma_2^{\infty}=-\sigma^{\infty}$), Eq. (35) can be rewritten as:

$$\frac{1}{2G_{eff}}(\sigma^{\infty})^2=\frac{1}{2G_m}(\sigma^{\infty})^2+W_1\frac{\phi}{\pi R^2},\tag{40}$$

where G_{eff} is the effective shear modulus of the composite, G_m is the shear modulus of the solid matrix, and W_1 is the excess energy under the shear load. Corresponding coefficients of the displacement fields in W_1 can be obtained from the results presented in

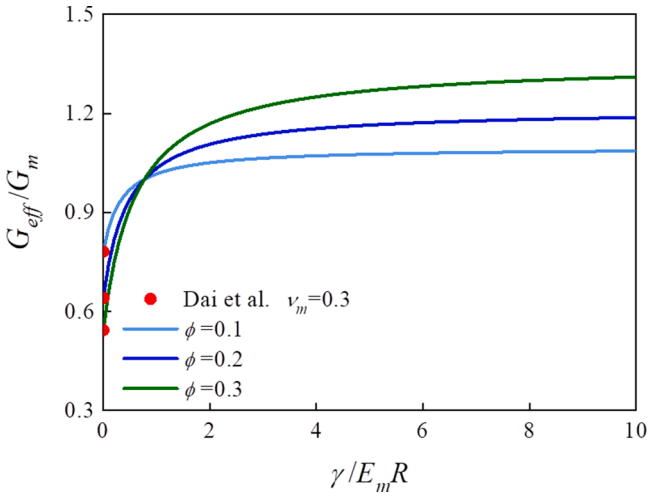

Fig. 7. Surface effects on effective shear modulus of a composite containing sparsely distributed cylindrical compressible liquid inclusions. Different colors represent different volume fractions of liquid inclusions. The effective shear modulus increases with increasing surface energy. Given that the liquid cannot bear shear force, the composite with liquid inclusions can be considered as a porous material with cavities. When surface tension becomes negligibly small, the present prediction reduces to existing result (Dai et al., 2020). For the plotting, $\nu_m = 0.3$.

Appendix B by setting $\sigma_1^\infty = \sigma^\infty$, $\sigma_2^\infty = -\sigma^\infty$. It follows from Eq. (40) that the normalized effective shear modulus is given by:

$$\frac{G_{eff}}{G_m} = \frac{1 - \left(-5 + \nu_m + 6\nu_m^2\right)\frac{\gamma}{E_m R}}{1 + 4(1-\nu_m)\phi + (1+\nu_m)[5 - 4\phi - (6-4\phi)\nu_m]\frac{\gamma}{E_m R}}. \tag{41}$$

The predicted surface effects on effective shear modulus are presented in Fig. 7 for selected volume fractions of liquid inclusions. For validation, the present results are compared with the existing results (Dai et al., 2020) when surface effects are absent ($\gamma/E_mR = 0$), with excellent agreement achieved. The effective shear modulus increases with increasing surface energy. Under far field shear loading, the volume of liquid inclusion remains unchanged, for the shear loading is equivalent to traction in one direction and compression in the other direction. Correspondingly, the cross-sectional area of the 2D liquid inclusion remains unchanged. However, the isoperimetric principle dictates that the perimeter of its surface must become longer after far field shear load is applied. The surface can store energy, thus needs to do work against surface forces when the surface area becomes larger. Therefore, increasing the surface energy reduces the shear strain, thus increasing the shear modulus. Further, it is observed from Fig. 7 that three lines intersect at one point where $G_{eff}/G_m = 1$. This implies that surface tension has the same influence on the deformation of a composite containing inclusions within a solid matrix. On the left side of the intersection point, the volume fraction of solid matrix is dominant for the effective shear modulus. In contrast, on its right side, the volume fraction (i.e., cross-sectional area) of liquid inclusion plays a dominant role, wherein surface effects stiffen the solid containing distributed liquid inclusions.

5.3. *Effective Young's modulus and Poisson ratio*

When the far field load is uniaxial stretching (i.e., $\sigma_1^\infty = \sigma^\infty$, $\sigma_2^\infty = 0$), Eq. (35) can be rewritten as:

$$\frac{1}{2E_{eff}}\left(1-\nu_{eff}^2\right)(\sigma^\infty)^2 = \frac{1}{2E_m}\left(1-\nu_m^2\right)(\sigma^\infty)^2 + W_2\frac{\phi}{\pi R^2}, \tag{42}$$

where W_2 is the excess energy due to a single liquid inclusion under far field uniaxial stretching. Corresponding coefficients of the displacement field can be obtained from Eq. (33).

Under biaxial stretching (i.e., $\sigma_1^\infty = \sigma^\infty$, $\sigma_2^\infty = \sigma^\infty$), Eq. (35) becomes:

$$\frac{1}{E_{eff}}\left(1-\nu_{eff}-2\nu_{eff}^2\right)(\sigma^\infty)^2 = \frac{1}{E_m}\left(1-\nu_m-2\nu_m^2\right)(\sigma^\infty)^2 + W_3\frac{\phi}{\pi R^2}, \tag{43}$$

where W_3 is the excess energy due to a single liquid inclusion subjected to far field biaxial stretching. Corresponding coefficients of the displacement field can be obtained from the Appendix B by setting $\sigma_1^\infty = \sigma_2^\infty = \sigma^\infty$.

Combination of (42) and (43) enables expressing explicitly the effective Young's modulus E_{eff} as:

$$\begin{aligned}\frac{E_{eff}}{E_m}=&\left[-1+\left(-5+\nu_m+6\nu_m^2\right)\frac{\gamma}{E_mR}\right]\left\{(1+\nu_m)\left[-1+\left(-5+\nu_m+6\nu_m^2\right)\frac{\gamma}{E_mR}\right]\right.\\&\left[-1+(1+\nu_m)\left(\frac{\gamma}{E_mR}-2\frac{K_i}{E_m}\right)\right]+(-1+\nu_m)\phi\\&\left[-5+(1+\nu_m)^2\left(-1-16\nu_m+12\nu_m^2\right)\left(\frac{\gamma}{E_mR}\right)^2\right.\\&+2\left(-7-5\nu_m+2\nu_m^2\right)\frac{K_i}{E_m}-2(1+\nu_m)(-9+4\nu_m)\frac{\gamma}{E_mR}\\&\left.+2(1+\nu_m)\left(1+17\nu_m+4\nu_m^2-12\nu_m^3\right)\frac{\gamma}{E_mR}\frac{K_i}{E_m}\right]\Big\}\\&\Big/\left\{(1+\nu_m)\left[-1+(1+\nu_m)\left(\frac{\gamma}{E_mR}-2\frac{K_i}{E_m}\right)\right]\right.\\&\left.\left[1+4(1-\nu_m)\phi+(1+\nu_m)(5-6\nu_m)-4\left(1-\nu_m^2\right)\phi\frac{\gamma}{E_mR}\right]^2\right\},\end{aligned}\tag{44}$$

and the effective Poisson ratio ν_{eff}as:

$$\begin{aligned}\nu_{eff}=&-\nu_m\left[-1+\left(-5+\nu_m+6\nu_m^2\right)\frac{\gamma}{E_mR}\right]\left[-1+(1+\nu_m)\left(\frac{\gamma}{E_mR}-2\frac{K_i}{E_m}\right)\right]\\&+(1-\nu_m)\left[-1+(1+\nu_m)^2\left(3-16\nu_m+12\nu_m^2\right)\left(\frac{\gamma}{E_mR}\right)^2\right.\\&+2(2\nu_m-3)(\nu_m+1)\frac{K_i}{E_m}+2(1+\nu_m)(5-4\nu_m)\frac{\gamma}{E_mR}\\&\left.-2(1+\nu_m)\left(3-13\nu_m-4\nu_m^2+12\nu_m^3\right)\frac{\gamma}{E_mR}\frac{K_i}{E_m}\right]\phi\\&\Big/\left\{\left[1+4(1-\nu_m)\phi+(1+\nu_m)(5-6\nu_m)-4\left(1-\nu_m^2\right)\phi\frac{\gamma}{E_mR}\right]\right.\\&\left.\left[-1+(1+\nu_m)\left(\frac{\gamma}{E_mR}-2\frac{K_i}{E_m}\right)\right]\right\}.\end{aligned}\tag{45}$$

For the case of cylindrical cavities with $\phi \ll 1$, the effective Young's modulus and Poisson ratio reduce to:

$$\frac{E_{eff}}{E_m}=1+\frac{(-1+\nu_m)\left[3+8\nu_m+2(1+\nu_m)(1-12\nu_m)\frac{\gamma}{E_mR}+(1+\nu_m)^2\left(7-8\nu_m+12\nu_m^2\right)\left(\frac{\gamma}{E_mR}\right)^2\right]}{(1+\nu_m)\left[-1+(1+\nu_m)\frac{\gamma}{E_mR}\right]\left[-1+(1+\nu_m)(-5+6\nu_m)\frac{\gamma}{E_mR}\right]}\phi,\tag{46}$$

$$\nu_{eff}=\nu_m+\frac{(-1+\nu_m)\left[-1+4\nu_m+2(1+\nu_m)(5-8\nu_m)\frac{\gamma}{E_mR}+3(1+\nu_m)^2(1-2\nu_m)^2\left(\frac{\gamma}{E_mR}\right)^2\right]}{\left[-1+(1+\nu_m)\frac{\gamma}{E_mR}\right]\left[-1+(1+\nu_m)(-5+6\nu_m)\frac{\gamma}{E_mR}\right]}\phi.\tag{47}$$

For the case of incompressible liquid inclusions when $\phi \ll 1$ we have:

$$\frac{E_{eff}}{E_m}=1+\frac{(1-\nu_m)\left[(1+10\nu_m)-(1+\nu_m)\left(7-8\nu_m+12\nu_m^2\right)\frac{\gamma}{E_mR}\right]}{(1+\nu_m)\left[-1+(1+\nu_m)(-5+6\nu_m)\frac{\gamma}{E_mR}\right]}\phi,\tag{48}$$

$$\nu_{eff}=\nu_m+\frac{3(1-\nu_m)(1-2\nu_m)\left[1+(1-2\nu_m)(1+\nu_m)\frac{\gamma}{E_mR}\right]}{1+(1+\nu_m)(5-6\nu_m)\frac{\gamma}{E_mR}}\phi.\tag{49}$$

Figure 8(a) presents the predicted surface effects on effective Poisson ratio for selected liquid bulk moduli: the effective Poisson ratio decreases with increasing surface energy. When the surface energy becomes sufficiently large (the precise value depending upon the mechanical properties of liquid and solid) and the deforming liquid inclusion remains stable, the composite with sparsely distributed cylindrical liquid inclusions exhibits a negative effective Poisson ratio. The underlying physical mechanism is identical to that associated with the auxetic effect discussed above in Section 4.1. The influence of liquid compressibility on effective Poisson ratio

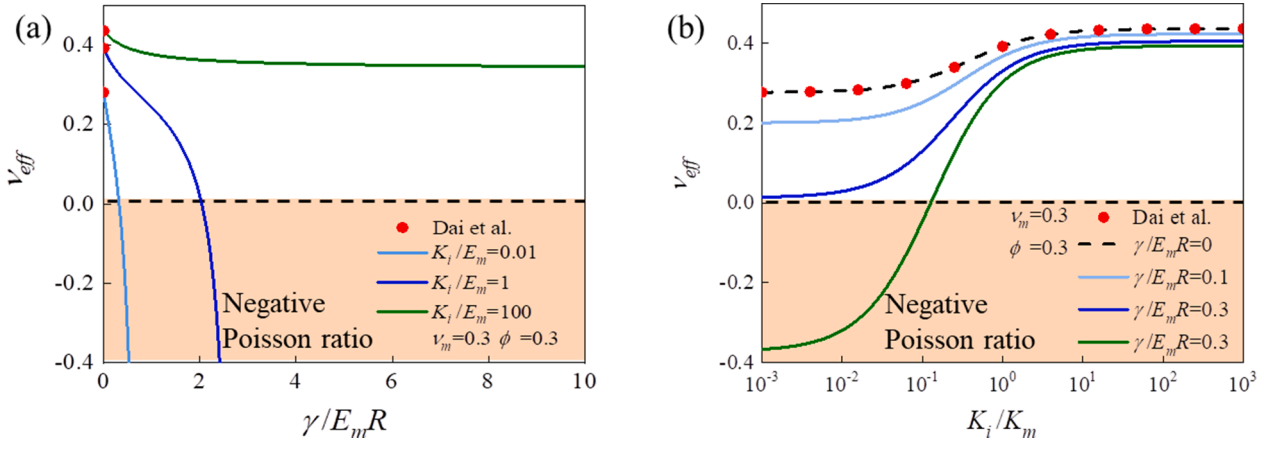

Fig. 8. Dependence of effective Poisson ratio on surface energy and liquid compressibility. (a) Surface effects. Different colors represent different bulk moduli of the liquid. The effective Poisson ratio decreases with increasing surface energy. When the surface energy is large enough (the value depends on the mechanical properties of solid matrix and liquid) but the material is still stable (i.e., $\frac{\gamma}{RE_m} < \frac{1}{1+\nu_m} + 2\frac{K_i}{E_m}$), the effective Poisson ratio becomes negative. (b) Influence of liquid compressibility. Different colors represent different surface energy densities. The effective Poisson ratio increases with increasing bulk modulus of the liquid. In the absence of surface tension, the prediction reduces to existing result obtained using a dilute model (Dai et al., 2020). For the plotting, $\nu_m = 0.3$ and $\phi = 0.3$ are selected.

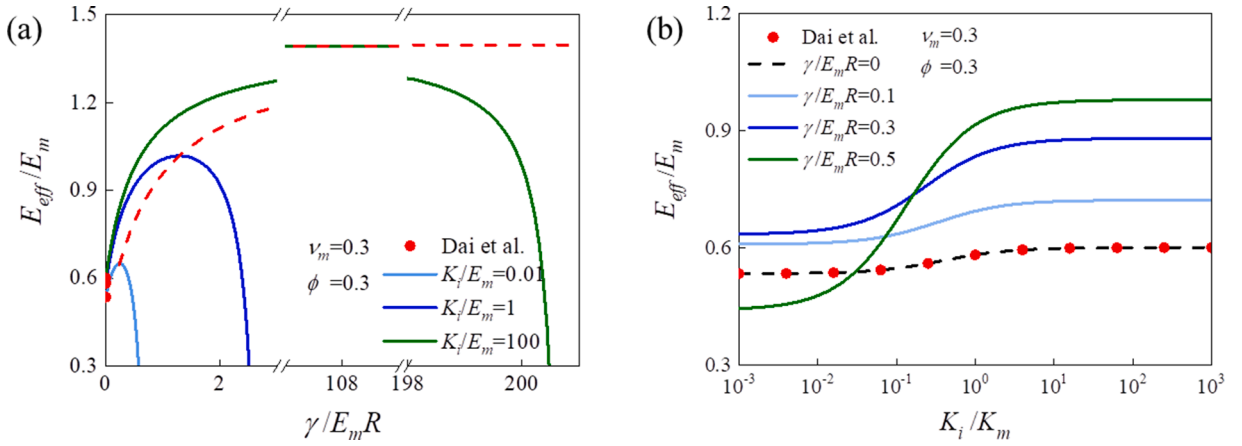

Fig. 9. Dependence of effective Young's modulus on surface energy and liquid compressibility. (a) Surface effects. The effective Young's modulus first increases and then decreases as surface energy is increased. Different colors represent different bulk moduli of the liquid. The red dashed line displays how the maximum effective Young's modulus varies with γ/E_mR for different bulk moduli of liquid. (b) Influence of liquid compressibility. Different colors represent different surface energy densities. The effective Young's modulus increases with increasing bulk modulus of the liquid. In the absence of surface tension, the prediction reduces to existing result obtained using a dilute model (Dai et al., 2020). For the plotting, $\nu_m = 0.3$ and $\phi = 0.3$ are selected.

is displayed in Fig. 8(b) for selected values of dimensionless surface energy. The effective Poisson ratio increases as the liquid bulk modulus is increased, for the lager the liquid bulk modulus, the harder it is for the far field load to change the liquid volume, thus affecting the effective Poisson ratio. Further, it is observed from Figs. 8(a, b) that the smaller the liquid bulk modulus, the easier to change the effective Poisson ratio from positive to negative by tailoring the surface effects. When surface tension is negligible ($\gamma/E_mR = 0$), the effective Poisson ratio is consistent with the existing result (Dai et al., 2020).

For selected liquid bulk moduli, Fig. 9(a) displays the variation trend of effective Young's modulus with surface tension, which first increases and then decreases as surface energy is increased. To explain such variation trend, we note that

$$E_{eff} = 2G_{eff}\left(1+\nu_{eff}\right). \tag{50}$$

The effective shear modulus for the case of low liquid compressibility (e.g.,$K_i/E_m = 0.01$) is given by:

$$G_{eff} = G_0 + k_G G_m \frac{\gamma}{E_m R} + o\left(\frac{\gamma}{E_m R}\right) \tag{51}$$

where G_0 is the effective shear modulus of the composite without surface effects, andk_G is the slope corresponding to small dimensionless surface energy, which is positive. Similarly, the effective Poisson ratio for low liquid compressibility (e.g.,$K_i/E_m = 0.01$) can be written as:

$$\nu_{eff} = \nu_0 + k_\nu \frac{\gamma}{E_m R} + o\left(\frac{\gamma}{E_m R}\right), \tag{52}$$

where ν_0 is the effective shear modulus without surface effects, and k_ν is the slope corresponding to small dimensionless surface energy, which is negative. Then, upon using Eqs. (51) and (52), the effective Young's modulus for low liquid compressibility can be obtained as:

$$\begin{aligned} E_{eff} &= 2\left(G_0 + k_G G_m \frac{\gamma}{E_m R} + o\left(\frac{\gamma}{E_m R}\right)\right)\left(1+\nu_0 + k_\nu \frac{\gamma}{E_m R} + o\left(\frac{\gamma}{E_m R}\right)\right) \\ &= 2G_0(1+\nu_0) + 2\left[k_G G_m(1+\nu_0) + k_\nu G_0\right]\frac{\gamma}{E_m R} + 2k_G k_\nu G_m\left(\frac{\gamma}{E_m R}\right)^2 + o\left(\left(\frac{\gamma}{E_m R}\right)^2\right), \end{aligned} \tag{53}$$

where $2G_0(1+\nu_0) = E_0$ is the effective Young's modulus without surface tension. Note that $2k_G k_\nu G_m$ is negative (which explains why the effective Young's modulus can decrease with increasing surface energy), and also that the axis of symmetry of the function $-\frac{k_G G_m(1+\nu_0)+k_\nu G_0}{2k_G k_\nu G_m}$ is positive. Therefore, the reason why the effective Young's modulus for the case of low liquid bulk modulus (e.g., $K_i/E_m = 0.01$) exhibits a variation trend as shown in Fig. 9(a) has been explained.

For larger liquid bulk moduli, the effective Young's moduli exhibit a similar variation trend to that of $K_i/E_m = 0.01$ (Fig. 9(a)): consistently, there exists a maximum effective Young's modulus, which has also been observed in previous studies on auxetic materials embedded with ellipsoidal or elliptic inclusions (Shufrin et al., 2015; Wei and Edwards, 1999a, b). The critical value of γ/E_mR that

maximizes the effective Young's modulus can be obtained by solving:

$$\frac{\partial E_{eff}}{\partial(\gamma/E_mR)} = 0. \tag{54}$$

The red dashed line shown in Fig. 9(a) displays how the maximum effective Young's modulus varies with γ/E_mR. To show more details of the curves in Fig. 9(a), we chose three regimes of the abscissa. For either $K_i/E_m = 0.01$ or $K_i/E_m = 100$, the value of γ/E_mR that maximizes the effective Young's modulus falls within the left regime. For $K_i/E_m = 100$, the value of γ/E_mR maximizing the effective Young's modulus is located in the middle regime, which is about $\gamma/E_mR = 108$. In the right regime, the effective Young's modulus for the case of large liquid bulk moduli (i.e., $K_i/E_m > 100$) tends to a limit.

The presence of maximum effective Young's modulus is helpful for constructing high-stiffness auxetic composites. In passing, we note that when γ/E_mR is further increased beyond its critical value and becomes sufficiently large, the effective Young's modulus drops below that obtained for the classical case of no surface effects (i.e., $\gamma/E_mR = 0$): this phenomenon has also been captured in previous studies (Wei and Edwards, 1999a).

For selected values of dimensionless surface energy (γ/E_mR), the influence of liquid compressibility on effective Young's modulus is depicted in Fig. 9(b). Generally speaking, the effective Young's modulus is seen to increase with increasing liquid bulk modulus: that is, the larger the liquid bulk modulus, the harder the composite is to be stretched. Nonetheless, when the dimensionless surface energy becomes sufficiently large (e.g., $\gamma/E_mR = 0.5$), the effective Young's modulus in the regime of low liquid bulk modulus (e.g., $K_i/E_m = 0.01$) can drop below that in the limiting case of no surface effects (i.e., $\gamma/E_mR = 0$). This interesting result indicates that combining sufficiently low dimensionless liquid bulk modulus (K_i/E_m) with sufficiently high dimensionless surface energy (γ/E_mR) enables designing softened composite materials with liquid inclusions. Note also that, in the limiting case $\gamma/E_mR = 0$ the present prediction coincides with that previously reported (Dai et al., 2020).

6. Discussion

Auxetic materials (i.e., materials with negative Poisson ratio) exhibit unique properties relative to conventional materials, such as larger shear modulus, enhanced indentation resistance, enlarged energy absorbance, higher fracture toughness, and enhanced crack growth resistance (Assidi and Ganghoffer, 2012; Wang et al., 2016). Representative auxetic materials in nature include silicon dioxide (SiO_2) in the α-cristobalite structure (Yeganeh-Haeri et al., 1992), skin tissue (Lees et al., 1991) and pyrolytic graphite (Novak et al., 2016). Representative man-made auxetic materials include two-dimensional honeycombs (Evans et al., 1991; Qin and Qin, 2020), three-dimensional cellular foams (Lakes, 1987; Zhang and Xiong, 2018) and microporous polymers (Caddock and Evans, 1989; Evans and Caddock, 1989). According to the results presented in Sections 4.1 and 5.2.2, we can construct novel composites with negative Poisson ratios by tailoring the dimensionless surface energy γ/E_mR. Further, we can tailor γ/E_mR to maximize the effective Young's modulus of the composite. Still further, according to the results of Section 4.2, we can tailor the dimensionless liquid compressibility K_i/E_m to minimize stress concentration around a liquid inclusion for enhanced composite strength. In a word, the present results provide useful guidelines for designing novel composite materials with unique attributes.

Cylindrical liquid inclusions are commonly found in biological tissues, such as dentin tubules, blood capillaries, and neuronal axons. For tissues with blood capillaries, the liquid phase is the blood and the solid matrix is the extracellular matrix (ECM), which provide structural and biochemical support to cells. The mechanics of ECM significantly influences cell behaviors and tissue developments (Peyton et al., 2007; Zheng et al., 2019), and hence characterizing its mechanical properties is critically important. Typically, the effective mechanical properties of tissue can be measured using a variety of experimental methods. Then, using the theoretical model developed in the current study, we can determine the mechanical properties of the ECM and investigate how they affect cell behaviors. Besides, the proposed model enables quantifying the influence of elastic fields in ECM on cell.

According to existing study (Chen et al., 2021), a solid matrix containing spherical liquid inclusions can be considered as a special kind of porous medium. Therefore, a solid matrix containing cylindrical liquid inclusions can also be considered as a special porous medium, which is transverse isotropic. Typically, for transversely isotropic porous media, eight poromechanical parameters are involved in constitutive modeling. In the current study, we have determined the effective mechanical properties of a composite with cylindrical liquid inclusions, which can be taken as its in-plane poromechanical coefficients. The out-of-plane poromechanical coefficients of the transversely isotropic composite will be presented in our follow-up studies.

7. Conclusion

A theoretical model has been developed to analyze the elastic field of a cylindrical compressible liquid inclusion and estimate the effective mechanical properties of a composite containing sparsely distributed cylindrical liquid inclusions, with surface effects duly accounted for. Different from previous studies, the linear dependence of the normal vector and curvature of liquid-solid surface upon deformation is considered in our model. Main results obtained are summarized below.

(1) Upon deformation, the cylindrical compressible liquid inclusion exhibits three distinct states: normal state, auxetic state and unstable (singular) state. Interplay between the liquid bulk modulus and surface energy dictates the boundary between the normal and auxetic states as well as the boundary between the auxetic and singular states.

(2) Previous studies of the cylindrical liquid inclusion did not predict its instability when the surface energy becomes sufficiently large, for the dependence of surface curvature on deformation was oversimplified in these studies.

(3) Stress concentration around the cylindrical liquid inclusion is minimized when the liquid bulk modulus has the same order of magnitude relative to the Young's modulus of the solid matrix, which is commonly found in biological systems.

(4) When surface energy is sufficiently large, the composite containing cylindrical liquid inclusions becomes auxetic, exhibiting negative effective Poisson ratio.

(5) The effective Young's modulus of the composite first increases and then decreases with increasing surface energy, and the transition point of the maximum effective Young's modulus is dependent upon the liquid bulk modulus.

The model given in the present study demonstrates significant surface effects on the elastic fields of cylindrical compressible liquid inclusion and provides useful guidelines for designing high-strength auxetic composite materials.

8. Author statement

Fei Ti: Methodology, Formal analysis, Writing - Original Draft Xin Chen: Methodology, Supervision Writing - Original Draft Moxiao Li: Visualization Writing - Review & Editing Xuechao Sun: Visualization Writing - Review & Editing Shaobao Liu: Visualization Writing - Review & Editing Tian Jian Lu: Supervision Writing - Review & Editing Funding acquisition

Declaration of Competing Interest

The authors declare that they have no known competing financial interests or personal relationships that could have appeared to influence the work reported in this paper.

Acknowledgements

This work was supported by the National Natural Science Foundation of China (12032010, 11902155), by the Natural Science Foundation of Jiangsu Province (BK20190382), by the Foundation for the Priority Academic Program Development of Jiangsu Higher Education Institutions.

Appendix A. Effect of liquid compressibility on displacement under uniaxial stretch

When subjected to far field uniaxial stretching in the x-direction, the displacement of point B (Fig. 1) decreases with increasing liquid bulk modulus for a given surface energy. Alternatively, with the liquid bulk modulus fixed, the displacement of point B increases with increasing surface energy, because surface tension tends to minimize surface area. Therefore, for the present 2D cylindrical liquid inclusions (more details presented in Section 4.1), the surface of the inclusion tends to a circle. In the limiting condition when surface tension vanishes (i.e., $\gamma/E_mR \to 0$), the present predictions coincide with existing solutions (red circles in Fig. A1) (Berli et al., 2006).

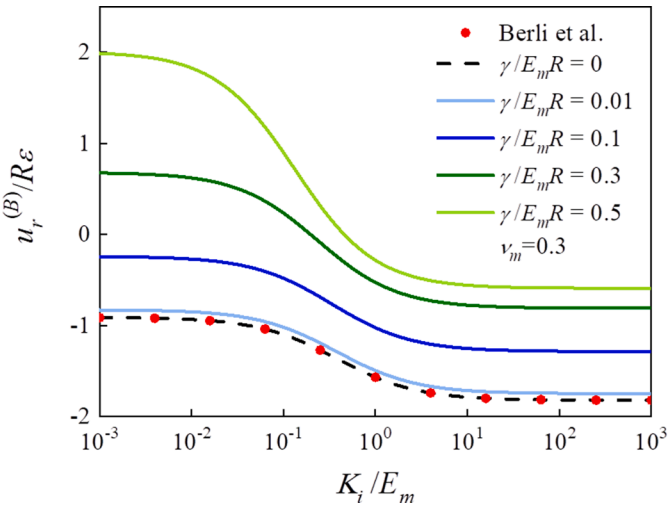

Fig. A1. Effect of liquid compressibility on displacement of point B (Fig. 1) under far field uniaxial stretch. Different colors represent different levels of surface energy. Red circles are existing results without surface tension (Berli et al., 2006). $\nu_m = 0.3$ is selected for the plotting.

Appendix B. The solution for biaxial stretch

When subjected to far field biaxial stretching (i.e., $\sigma_{xx}^{\infty} = \sigma_1^{\infty}, \sigma_{yy}^{\infty} = \sigma_2^{\infty}$), the coefficients of the elastic fields are:

$$B_1 = \frac{1-\nu_m-2\nu_m^2}{2}\frac{\sigma_1^{\infty}+\sigma_2^{\infty}}{E_m},$$

$$B_2 = \frac{(1+\nu_m)\left[\left(-1+\nu_m+2\nu_m^2\right)\left(\frac{L}{R}-2\frac{K_i}{E_m}\right)-1\right]}{2\left[(1+\nu_m)\left(\frac{L}{R}-2\frac{K_i}{E_m}\right)-1\right]}\frac{\sigma_1^{\infty}+\sigma_2^{\infty}}{E_m},$$

$$A_1 = 0,$$

$$A_2 = -\frac{(1+\nu_m)}{4}\frac{\sigma_1^{\infty}-\sigma_2^{\infty}}{E_m},$$

$$A_3 = \frac{(1+\nu_m)\left[(1+\nu_m)\frac{L}{R}-1\right]}{2\left[\left(-5+\nu_m+6\nu_m^2\right)\frac{L}{R}-1\right]}\frac{\sigma_1^{\infty}-\sigma_2^{\infty}}{E_m},$$

$$A_4 = -\frac{(1+\nu_m)\left[\left(-1+\nu_m+2\nu_m^2\right)\frac{L}{R}-1\right]}{4\left[\left(-5+\nu_m+6\nu_m^2\right)\frac{L}{R}-1\right]}\frac{\sigma_1^{\infty}-\sigma_2^{\infty}}{E_m}.$$

Reference

Armstrong, R., Phelps, R., 1984. Muscle fiber type composition of the rat hindlimb. Am. J. Anat. 171, 259–272.

Assidi, M., Ganghoffer, J.F., 2012. Composites with auxetic inclusions showing both an auxetic behavior and enhancement of their mechanical properties. Compos. Struct. 94, 2373–2382.

Bejan, A., 1999. How nature takes shape: extensions of constructural theory to ducts, rivers, turbulence, cracks, dendritic crystals and spatial economics. Int. J. Therm. Sci. 38, 653–663.

Bejan, A., 2000. Shape and structure, from Engineering to Nature. Cambridge university press, Cambridge.

Berli, M., Eggers, C., Accorsi, M., Or, D., 2006. Theoretical analysis of fluid inclusions for in situ soil stress and deformation measurements. Soil Sci. Soc. Am. J. 70, 1441–1452.

Britannica, E., 1993 . Encyclopædia britannica. University of Chicago, Chicago.

Caddock, B., Evans, K., 1989. Microporous materials with negative Poisson's ratios. I. Microstructure and mechanical properties. J. Phys. D: Appl. Phys. 22, 1877–1882.

Chakrabarti, A., Chaudhury, M.K., 2013. Direct measurement of the surface tension of a soft elastic hydrogel: exploration of elastocapillary instability in adhesion. Langmuir 29, 6926–6935.

Cheewaruangroj, N., Leonavicius, K., Srinivas, S., Biggins, J.S., 2019. Peristaltic elastic instability in an inflated cylindrical channel. Phys. Rev. Lett. 122, 068003.

Chen, X., Li, M., Yang, M., Liu, S., Genin, G.M., Xu, F., Lu, T.J., 2018. The elastic fields of a compressible liquid inclusion. Extreme Mech. Lett. 22, 122–130.

Chen, X., Ti, F., Li, M., Liu, S., Lu, T.J., 2021. Theory of fluid saturated porous media with surface effects. J. Mech. Phys. Solids 151, 104392.

Cheng, Z.-Q., Batra, R., 1999. Exact Eshelby tensor for a dynamic circular cylindrical inclusion. J. Appl. Mech. 66, 563–565.

Christensen, R.M., Lo, K.H., 1979. Solutions for effective shear properties in three phase sphere and cylinder models. J. Mech. Phys. Solids 27, 315–330.

Chuanren, D., Bochu, W., Pingqing, W., Daohong, W., Shaoxi, C., 2004. Relationship between the minute structure and the lodging resistance of rice stems. Colloids Surf. B: Biointerfaces 35, 155–158.

Dai, M., Hua, J., Schiavone, P., 2020. Compressible liquid/gas inclusion with high initial pressure in plane deformation: modified boundary conditions and related analytical solutions. Eur. J. Mech. A/Solid 82, 104000.

Dai, M., Li, M., Schiavone, P., 2018. Plane deformations of an inhomogeneity–matrix system incorporating a compressible liquid inhomogeneity and complete Gurtin–Murdoch interface model. J. Appl. Mech. 85, 121010.

Dai, M., Yang, H.-B., Schiavone, P., 2019. Stress concentration around an elliptical hole with surface tension based on the original Gurtin–Murdoch model. Mech. Mater. 135, 144–148.

Do Carmo, M.P., 1976. Differential Geometry of Curves and Surfaces. Prentice-Hall, Englewood Cliffs.

Duan, H.L., Wang, J., Huang, Z.P., Karihaloo, B.L., 2005. Size-dependent effective elastic constants of solids containing nano-inhomogeneities with interface stress. J. Mech. Phys. Solids 53, 1574–1596.

Duan, H.L., Yi, X., Huang, Z.P., Wang, J., 2007. A unified scheme for prediction of effective moduli of multiphase composites with interface effects. Part I: theoretical framework. Mech. Mater. 39, 81–93.

Eshelby, J., 1956. The continuum theory of lattice defects. Solid State Phys 3, 79–144.

Eshelby, J.D., 1957. The determination of the elastic field of an ellipsoidal inclusion, and related problems. Proc. R. Soc. London, Ser. A 241, 376–396.

Evans, K., Caddock, B., 1989. Microporous materials with negative Poisson's ratios. II. Mechanisms and interpretation. J. Phys. D: Appl. Phys. 22, 1883–1887.

Evans, K.E., Nkansah, M.A., Hutchinson, I.J., Rogers, S.C., 1991. Molecular network design. Nature 353, 124, 124.

Fischer, F., Waitz, T., Vollath, D., Simha, N., 2008. On the role of surface energy and surface stress in phase-transforming nanoparticles. Prog. Mater. Sci. 53, 481–527.

Frame, J., Wheel, M., Riches, P., 2018. A numerical investigation and experimental verification of size effects in loaded bovine cortical bone. Int. J. Numer. Mech. Bio. 34, e2903.

Frolov, S., Potlov, A.Y., Frolova, T., Proskurin, S., 2019. Compression elastography and endoscopic optical coherence tomography for biomechanical properties evaluation of cerebral arteries walls with aneurysm and their phantoms. AIP Conf. Proc. 2140, 020020.

Frutiger, A., Muth, J.T., Vogt, D.M., Mengüç, Y., Campo, A., Valentine, A.D., Walsh, C.J., Lewis, J.A., 2015. Capacitive soft strain sensors via multicore–shell fiber printing. Adv. Mater. 27, 2440–2446.
Fuchs, Z., Scaal, M., Haverkamp, H., Koerber, F., Persigehl, T., Eifinger, F., 2018. Anatomical investigations on intraosseous access in stillborns-comparison of different devices and techniques. Resuscitation 127, 79–82.
Goodier, J.J.T., 1933. Concentration of stress around spherical and cylindrical inclusions and flaws. J. Appl. Mech. 55, 39–44.
Gurtin, M.E., Murdoch, A.I., 1975. A continuum theory of elastic material surfaces. Arch. Ration. Mech. An. 57, 291–323.
Harrison, R.V., Harel, N., Panesar, J., Mount, R.J., 2002. Blood capillary distribution correlates with hemodynamic-based functional imaging in cerebral cortex. Cereb. Cortex 12, 225–233.
Hasegawa, H., Lee, V.-.G., Mura, T., 1992. The stress fields caused by a circular cylindrical inclusion. J. Appl. Mech. 59, S107–S114.
Hasselman, D., Fulrath, R.M., 2010. Micromechanical stress concentrations in two-phase brittle-matrix ceramic composites. J. Am. Ceram. Soc. 50, 399–404.
He, L., Li, Z., 2006. Impact of surface stress on stress concentration. Int. J. Solids Struct. 43, 6208–6219.
Henann, D.L., Bertoldi, K., 2014. Modeling of elasto-capillary phenomena. Soft Matter 10, 709–717.
Huang, G., Zhang, X., Xiao, Z., Zhang, Q., Zhou, J., Xu, F., Lu, T.J., 2012. Cell-encapsulating microfluidic hydrogels with enhanced mechanical stability. Soft Matter 8, 10687–10694.
Huang, G.Y., Zhou, L.H., Zhang, Q.C., Chen, Y.M., Sun, W., Xu, F., Lu, T.J., 2011. Microfluidic hydrogels for tissue engineering. Biofabrication 3, 012001.
Huang, Z., Wang, J., 2013. Micromechanics of Nanocomposites With Interface Energy effect, Handbook of Micromechanics and Nanomechanics. Pan Stanford Publishing Pte. Ltd., Singapore, pp. 303–348.
Hwu, C., Ting, T., 1989. Two-dimensional problems of the anisotropic elastic solid with an elliptic inclusion. Q. J. Mech. Appl. Math. 42, 553–572.
In, J., Ryu, J., Yu, H., Kang, D., Kim, T., Kim, J., 2021. Microfluidic valvular chips and a numerical lymphatic vessel model for the study of lymph transport characteristics. Lab Chip 21, 2283–2293.
Jindal, P., Sharma, J., Bashir, R., 2016. Effect of pore-water surface tension on tensile strength of unsaturated sand. Indian Geotech. J. 46, 276–290.
Kolkman, R., Klaessens, J., Hondebrink, E., Hopman, J., Leeuwen, T., 2004. Photoacoustic determination of blood vessel diameter. Phys. Med. Biol. 49, 4745–4756.
Kosmopoulos, V., Keller, T.S., Schizas, C., 2009. Early stage disc degeneration does not have an appreciable affect on stiffness and load transfer following vertebroplasty and kyphoplasty. Eur. Spine J. 18, 59–68.
Krichen, S., Liu, L., Sharma, P., 2019. Liquid inclusions in soft materials: capillary effect, mechanical stiffening and enhanced electromechanical response. J. Mech. Phys. Solids 127, 332–357.
Lakes, R., 1987. Foam structures with a negative Poisson's ratio. Science 235, 1038–1041.
Lees, C., Vincent, J., Hillerton, J.E., 1991. Poisson's ratio in skin. Bio-Med. Mater. Eng. 1, 19–23.
Lin, M., Luo, Z.Y., Bai, B.F., Xu, F., Lu, T.J., 2011. Fluid mechanics in dentinal microtubules provides mechanistic insights into the difference between hot and cold dental pain. PLoS One 6, e18068.
Love, A., 1944. A Treatise On the Mathematical Theory of Elasticity. Cambridge University Press, Cambridge.
Mancarella, F., Style, R.W., Wettlaufer, J.S., 2016. Interfacial tension and a three-phase generalized self-consistent theory of non-dilute soft composite solids. Soft Matter. 12, 2744–2750.
Min, K.L., Rich, M.H., Baek, K., Lee, J., Kong, H., 2015. Bioinspired tuning of hydrogel permeability-rigidity dependency for 3D. Cell Culture. Sci. Rep.-UK 5, 1–7.
Mishnaevsky Jr,, L., Brøndsted, P., 2009. Micromechanical modeling of damage and fracture of unidirectional fiber reinforced composites: a review. Comp. Mater. Sci. 44, 1351–1359.
Mora, S., Phou, T., Fromental, J.-.M., Pismen, L.M., Pomeau, Y., 2010. Capillarity driven instability of a soft solid. Phys. Rev. Lett. 105, 214301.
Mutalik, S.P., Ghose, A., 2020. Axonal cytomechanics in neuronal development. J. Biosci. 45, 1–17.
Nix, W.D., Gao, H., 1998. An atomistic interpretation of interface stress. Scripta Mater 39, 1653–1661.
Novak, N., Vesenjak, M., Ren, Z., 2016. Auxetic cellular materials-a review. Stroj Vestn. J. Mech. Eng 62, 485–493.
Olszewski, W.L., Engeset, A., 1980. Intrinsic contractility of prenodal lymph vessels and lymph flow in human leg. Am. J. Physiol. Heart Circ. Physiol. 239, H775–H783.
Oshita, H., 2019. Mechanical characteristics for concrete as a permeable material based on coupled problem with solid, liquid and gas phases. In: COUPLED VIII: Proceedings of the VIII International Conference on Computational Methods for Coupled Problems in Science and Engineering, pp. 662–672.
Ou, Z., Wang, G., Wang, T., 2008. Effect of residual surface tension on the stress concentration around a nanosized spheroidal cavity. Int. J. Eng. Sci. 46, 475–485.
Ozcan, O., Gonul, B., Bulutcu, A., Manav, H., 2001. Correlations between the shear strength of mineral filter cakes and particle size and surface tension. Colloids Surf. Physicochem. Eng. Aspects 187, 405–413.
Peyton, S.R., Ghajar, C.M., Khatiwala, C.B., Putnam, A.J., 2007. The emergence of ECM mechanics and cytoskeletal tension as important regulators of cell function. Cell Biochem. Biophys. 47, 300–320.
Qin, G., Qin, Z., 2020. Negative Poisson's ratio in two-dimensional honeycomb structures. npj Comput. Mater. 6, 1–6.
Rosina, J., Kvasnak, E., Suta, D., Kolarova, H., Malek, J., Krajci, L., 2007. Temperature dependence of blood surface tension. Physiol. Res. 56, S93–S98.
Ru, Y., Wang, G., Wang, T., 2009. Diffractions of elastic waves and stress concentration near a cylindrical nano-inclusion incorporating surface effect. J. Vib. Acoust. 131, 061011.
Sarin, H., 2010. Physiologic upper limits of pore size of different blood capillary types and another perspective on the dual pore theory of microvascular permeability. J. Angiogenes. Res. 2, 1–19.
Shafiro, B., Kachanov, M., 1997. Materials with fluid-filled pores of various shapes: effective elastic properties and fluid pressure polarization. Int. J. Solids Struct. 34, 3517–3540.
Sharma, P., Ganti, S., Bhate, N., 2003. Effect of surfaces on the size-dependent elastic state of nano-inhomogeneities. Appl. Phys. Lett. 82, 535–537.
Shufrin, I., Pasternak, E., Dyskin, A.V., 2015. Hybrid materials with negative Poisson's ratio inclusions. Int. J. Eng. Sci. 89, 100–120.
Style, R.W., Wettlaufer, J.S., Dufresne, E.R., 2015. Surface tension and the mechanics of liquid inclusions in compliant solids. Soft. Matter. 11, 672–679.
Timoshenko, S., Goodier, J.N., 1951. The Theory of Elasticity. McGraw-Hill, New York.
Van Mechelen, J., 2004. Strength of moist sand controlled by surface tension for tectonic analogue modelling. Tectonophysics 384, 275–284.
Vutukuri, V., 1974. The effect of liquids on the tensile strength of limestone. Int. J. Rock Mech. Min. Sci. Geomech. Abstr. 11, 27–29.
Wang, Z., Zulifqar, A., Hu, H., 2016. Auxetic composites in aerospace engineering. Adv. Compos. Mater. Aerosp. Eng 213–240.
Wei, G., Edwards, S., 1999a. Effective elastic properties of composites of ellipsoids (I). Nearly spherical inclusions. Physica A 264, 388–403.
Wei, G., Edwards, S., 1999b. Effective elastic properties of composites of ellipsoids (II). Nearly disk-and needle-like inclusions. Physica A 264, 404–423.
Wu, J., Ru, C., Zhang, L., 2018. An elliptical liquid inclusion in an infinite elastic plane. P. Roy. Soc. A-Math. Phy. 474, 20170813.
Xuan, C., Biggins, J., 2015. Finite wavelength surface-tension driven instabilities in soft solids. Phys. Rev. E 94, 023107.
Yang, F., 2004. Size-dependent effective modulus of elastic composite materials: spherical nanocavities at dilute concentrations. J. Appl. Phys. 95, 3516–3520.
Yeganeh-Haeri, A., Weidner, D.J., Parise, J.B., 1992. Elasticity of alpha-cristobalite: a silicon dioxide with a negative Poisson's ratio. Science 257, 650–652.
Zandim, D.L., Corrêa, F.O.B., Sampaio, J.E.C., Júnior, R.C., 2004. The influence of vinegars on exposure of dentinal tubules: a SEM evaluation. Braz. Oral Res. 18, 63–68.
Zhang, J., Xiong, Q., 2018. The negative Poisson's ratio in graphene-based carbon foams. Phys. Chem. Chem. Phys. 20, 4597–4605.
Zheng, Y., Nan, H., Fan, Q., Wang, X., Liu, L., Liu, R., Ye, F., Sun, B., Jiao, Y., 2019. Modeling cell migration regulated by cell extracellular-matrix micromechanical coupling. Phys. Rev. E 100, 043303.
Ziskind, D., Hasday, M., Cohen, S.R., Wagner, H.D., 2011. Young's modulus of peritubular and intertubular human dentin by nano-indentation tests. J. Struct. Biol. 174, 23–30.